Towards Realtime Classification of Optically Trapped Particles

Vicente V. Rocha
Mestrado em Física
Departamento de Física e Astronomia
2022

Orientador
Prof. Dr. Nuno Silva, INESC TEC, Faculdade de Ciências

Coorientador
Prof. Dr. Pedro Jorge, INESC TEC, Faculdade de Ciências
Prof. Dr. Ariel Guerreiro, INESC TEC, Faculdade de Ciências

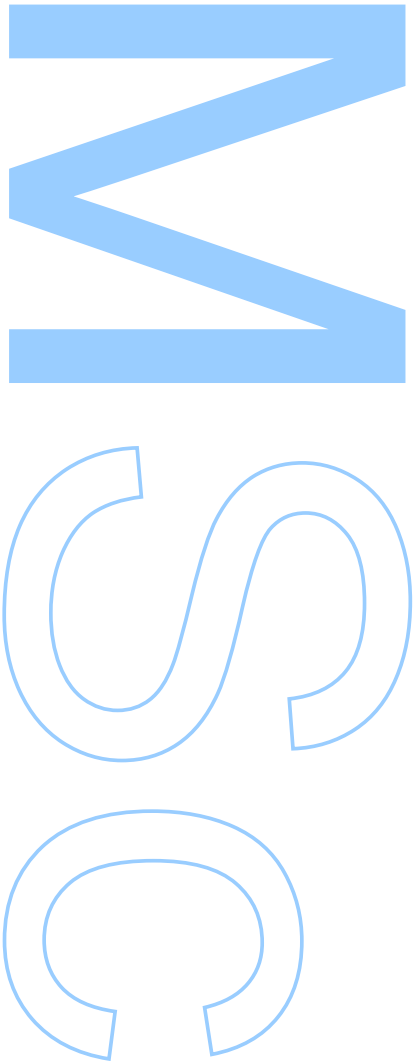

U.PORTO

FACULDADE DE CIÊNCIAS
UNIVERSIDADE DO PORTO

Todas as correções determinadas pelo júri, e só essas, foram efetuadas.

O Presidente do Júri,

Porto, _____/_____/_____

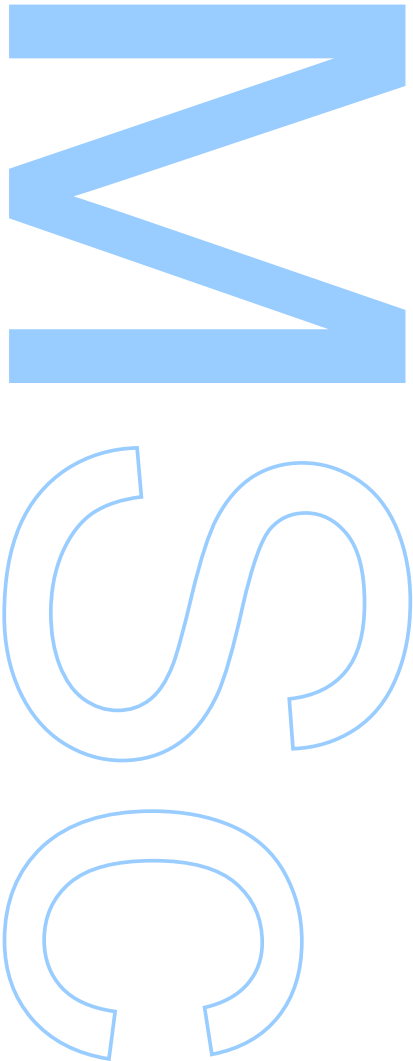

Sworn Statement

I, Vicente Vieira Rocha, enrolled in the Master Degree in Physics at the Faculty of Sciences of the University of Porto hereby declare, in accordance with the provisions of paragraph a) of Article 14 of the Code of Ethical Conduct of the University of Porto, that the content of this dissertation reflects perspectives, research work and my own interpretations at the time of its submission.

By submitting this dissertation, I also declare that it contains the results of my own research work and contributions that have not been previously submitted to this or any other institution.

I further declare that all references to other authors fully comply with the rules of attribution and are referenced in the text by citation and identified in the bibliographic references section. This dissertation does not include any content whose reproduction is protected by copyright laws.

I am aware that the practice of plagiarism and self-plagiarism constitute a form of academic offense.

Vicente Vieira Rocha

20/12/2022

UNIVERSIDADE DO PORTO

MASTERS THESIS

Towards Realtime Classification of Optically Trapped Particles

Author:
Vicente ROCHA

Supervisor:
Nuno SILVA

A thesis submitted in fulfilment of the requirements
for the degree of MSc. Physics

at the

Faculdade de Ciências da Universidade do Porto
Departamento de Física e Astronomia

December 20, 2022

Acknowledgements

Made of both victories and defeats, the development of this dissertation had the constant presence of hardships eased by the presence of family, friends and colleagues. To these people, i am grateful for the kind words, company and help.

First of all, to my advisors Dr. Pedro Jorge and Dr. Ariel Guerreiro who set the stage to realise this work and in particular to the main advisor and friend Dr. Nuno Silva who proactively and tirelessly accompanied me in the writing of this work. Also, i thank the team at the Center for Applied Photonics at INESC TEC namely Tiago Ferreira who advised, guided and helped me in a series of tasks.

Secondly, to my aunts, uncles, cousins and grandparents in Porto who in these last few years were a constant company and help that i could always rely on.

I would also like to thank my family in the city of Leiria, namely my grandparents who constantly should presence and helpfulness to give me courage and strength.

To my friends Rui Gândara, Beatriz Lopes, Fabrizio Dodat e Carolina Barbosa with whom i could always count in these last couple of years to encourage me to move forward.

Finally, leaving the most important for the end, i am grateful to my parents and my brother who have supported and provided a basis upon which i could reach this pivotal step in my life.

UNIVERSIDADE DO PORTO

Abstract

Faculdade de Ciências da Universidade do Porto
Departamento de Física e Astronomia

MSc. Physics

Towards Realtime Classification of Optically Trapped Particles

by Vicente ROCHA

In recent decades, optical tweezers(OT) have emerged as a powerful tool to work with micro-sized particles. Indeed, by allowing micromanipulation and analysis of a wide range of synthetic and biological particles, OT may impact a plethora of natural sciences ranging from biology to physics. Yet, in spite of its successes for fundamental research purposes, it still needs to solidify its role as a reliable and versatile technological tool. In particular, one of the most promising applications of OT is the classification of the optically trapped particles, but the existent methodologies still lack the necessary performance and throughput to be able to support high-performance diagnostic tools.

In this context, this work explores the implementation of machine learning algorithms capable of speeding up classification performance while maintaining accuracy, focusing for this purpose on two architectures: convolution neural networks(CNN) and reservoir computing(RC). In particular, the CNN framework takes advantage of the modern era graphic processing unit (GPU) for fast classification and, looking toward real-time execution, while RC explores the concept of recurrent neural networks for processing time series in a timely manner. We tested both frameworks on experimentally acquired time series for the forward scattered signal from an inverted microscope OT setup and measured with a quadrant photodetector. Furthermore, with the development of a digital twin, we were also capable of verifying the experimental results on synthetic data.

The case studies implemented looked to evaluate classification in both the composition and size characteristics of the particles. The results highlight the capabilities of CNNs for the fast classification of optically trapped particles, which as verified by both experimental and synthetic data with similar results. In contrast, RC only performed well for one of the datasets, which leaving room for future improvements.

In conclusion, this dissertation presents the use of two machine learning algorithms for the classification of trapped particles in OT setups, which to our best knowledge were unexplored in the literature. These present non-trivial opportunities, improving the throughput and performance of technological tools based on OT, while also paving for innovative solutions using RC that may be implemented in all-optical manners in future miniaturized integrated solutions.

UNIVERSIDADE DO PORTO

Resumo

Faculdade de Ciências da Universidade do Porto
Departamento de Física e Astronomia

Mestrado em Física

Rumo à classificação em tempo real de partículas opticamente presas

por Vicente ROCHA

Nas última décadas, as pinças óticas surgem como uma ferramenta importante para trabalhar com partículas de tamanho micrométrico. De facto, ao permitir manipular e analisar partículas micrométrica de uma ampla gama de partículas sintéticas e biológicas, pinças óticas podem impactar uma infinidade de ciências naturais desde biologia à física. No entanto, apesar dos seus sucessos para fins de pesquisa fundamental, ainda é preciso solidificar o seu papel como uma ferramenta confiável e versátil. Em particular, uma das aplicações mais promissoras de pinças óticas é a classificação de partículas oticament presas, mas as metodologias existentes ainda carecem de desempenho e eficiência necessária para poder suportar ferramentas de diagnóstico de alto desempenho.

Neste context, este trabalho explora a implementação de algoritmos inteligentes capazes de acelerar o desempenho da classificação mantendo a precisão, focando para este propósito em dois tipos de arquitetura: rede neuronal convolucional e computação de reservatório. Em particular, as redes neuronais convolucionais tomam vantagem das unidades de processamento gráfico da era moderna para classificação rápida e, com olhos postos na execução em tempo real, computação de reservatório explora o conceito de redes neuronais recorrentes para processamento direto de séries temporais. Testamos ambas as arquiteturas em séries temporais adquiridas experimentalmente do sinal disperso para a frente com recurso à configuração de microcópio invertido de pinças óticas integrado com um detetor de photões de quadrantes. Além disso, com o desenvolvimento de um gêmeo digital da montagem experimental, também fomos capazes de verificar os resultados experimentais em dados sintéticos.

Os estudos de caso implementados procuram avaliar a classificação com base tanto na composição quanto no tamanho das partículas. Os resultados destacam as capacidades das redes neuronais convolucionais para a classificação rápida de partículas oticamente presas, o que foi verificado com resultados semelhantes por dados experimentais e sintéticos. Em contraste, a computação de reservatório obteve apenas bom desempenho para um dos conjuntos de dados, o que deixa espaço para melhorias futuras.

Em conclusão, esta dissertação apresenta o uso de dois algoritmos inteligentes para a classificação de partículas aprisionadas em configurações de pinças óticas, os quais, no melhor do nosso conhecimento eram inexploradas na literatura. Estas oportunidades melhoram a velocidade e o desempenho de tecnologias baseadas em pinças óticas, ao mesmo tempo que abrem caminhos para soluções inovadora usando computação em reservatório que podem ser implementadas de forma totalmente óptica em futuras soluções integradas e miniaturizadas.

Contents

List of Figures

Glossary

CNN	Convolution Neural Network
RC	Reservoir Computing
3D	3-Dimensional
NA	Numerical Aperture
OT	Optical Tweezers
HOT	Holographic Optical Tweezers
SLM	Spatial Light Modulator
FOT	Fiber Optical Tweezers
PCA	Principal Component Analysis
SNR	Signal-To-Noise Ratio
DL	Deep Learning
GPU	Graphic Processor Unit
RNN	Recurrent Neural Networks
ESN	Echo State Networks
GO	Geometric Optics
CW	Continuous-Wave
MSD	Mean Squared Displacement
PSD	Power Spectral Density
RK4	Runge-Kutta 4
NN	Neural Network
ESP	Echo State Property

Chapter 1

Introduction

In a series of revolutionary reports starting from 1970, Arthur Ashkin[1] reshaped the toolbox for the experimental manipulation of particles with the development of Optical Tweezers[2, 3], eventually awarding him the Nobel prize later in 2018. Indeed, from multiple particle trapping[4] to single atoms[5] and cells[6], optical tweezers now find contributions to a plethora of natural sciences.

To provide some illustrative examples of the versatility of the tool, optical tweezers have been used in biology applications for a long time, namely to manipulate specimens and probe their dynamical properties in the laboratory[7]. In a distinct context, the same tool has been emerging for monitoring processes and reactions in chemistry applications and measuring the rheological properties of the medium[8–10]. Leaning towards the fundamental side of science and focusing on atomic and quantum physics, the same underlying concept supports the trapping of atomic clouds, which combined with other magnetic and optical solutions, allows the exploration of macroscopic quantum matter states at the micro to nano-kelvin scales[11–14].

Still, and in spite of all the solid academic applications, Optical Tweezers has still to solidify its role as a reliable and versatile technological solution. Pointing in this direction, the team of the Center for Applied Photonics at INESC TEC has been developing in the last 5 years a consistent effort for the development of intelligent, automatic, and fast Optical Tweezers systems for biological sensing purposes. In particular, the work has mostly focused on the classification and identification of trapped specimens, capable of identifying and distinguishing particles and cells[15, 16].

Nevertheless, the solutions and algorithms developed so far still require a significant time and computational load for signal acquisition and processing. This prevents the

use of systems that can give high throughput classification rates, which may be desirable for applications requiring this scan (e.g. ultra-low concentrations of the target particle or monitoring large volumes). In this context, this dissertation describes our efforts to deploy an ultra-fast and real-time solution for the identification of the trapped particle, starting from the first principles and covering state-of-the-art machine learning solutions like convolutional neural networks (CNN) and reservoir computing (RC) paradigms.

1.1 Optical tweezers: concepts and setups

The observation of optical forces dates back to Kepler, that proposed the existence of radiation pressure by observing that the tail of a comet consistently pointed away from the Sun. Later, more than 200 years after that, Maxwell introduced the momentum of the electromagnetic wave, providing a theoretical framework to explain how radiation fields are capable of exerting forces[17, 18]. Built upon these principles and driven by the invention of the laser, Ashkin and his colleagues reported the first observation of the trapping of transparent dielectric spheres in 1970[1].

This first optical trapping setup was suggested after the observation of a single beam scattering force pushing a particle along and a gradient force attracting it inwards towards higher intensities. By counterpropagating two beams, see figure 1.1.a, the scattering forces cancel out and an equilibrium position can be created[1]. Yet, the complexity of the setup forbade effective 3-dimensional (3D) manipulation. Not long after, a single beam optical trap was devised by counterbalancing radiation pressure against gravity[19]. Nevertheless, by allowing only levitation of particles this tool lacked versatility.

Later on, Ashkin introduced a novel "single-beam optical trap" paradigm, which leveraged on a single highly focused beam[20]. This technique uses the dipolar component of light-matter interaction to induce an optical gradient force that counters the scattering force and creates an equilibrium position, see figure 1.1.b. Finally, in 1986, the first optical tweezers setup was first reported in Optics Letters, a manuscript that to this day remains the most cited of this prestigious publication. Following a close concept to the theoretical prediction for atoms, they used a high numerical aperture (NA) objective to tightly focus the beam, generating higher intensity gradients and consequently stronger attractive gradient forces. By achieving a counterbalance between the radiation and gradient optical forces, an effective 3D trap is created, sparking the subject that we now know as Optical Tweezers (OT)[2].

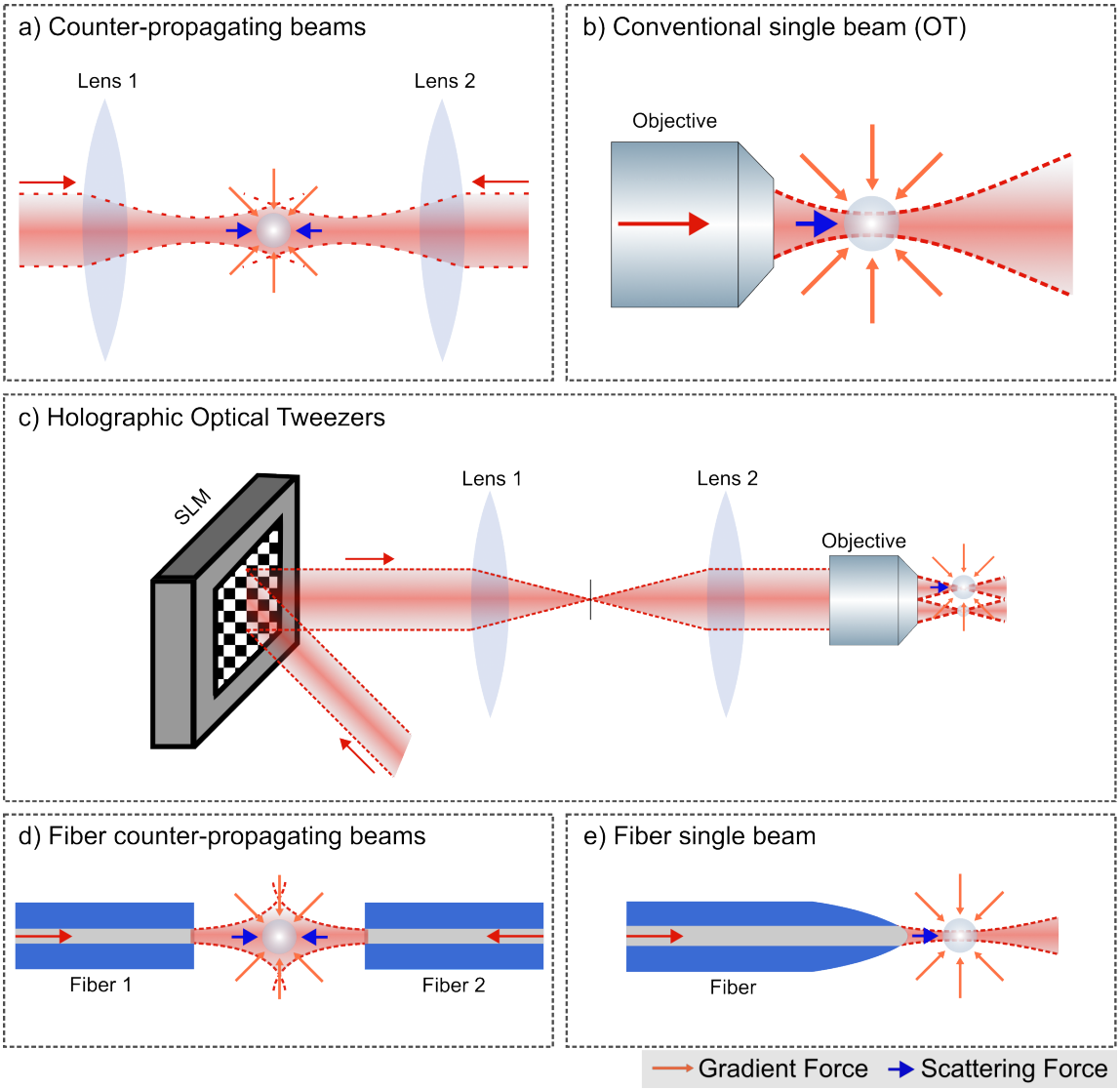

FIGURE 1.1: Illustrative example of optical manipulators with the representation of the forward-pushing scattering forces (blue arrow) and restoring gradient forces (orange arrow) exerted on the trapped particle. By cancelling scattering forces using counter-propagating beams, the conventional configuration (a) and fiber application (d) leverage on the gradient forces to effectively trap particles. In the single beam configuration, the conventional setup (b) and fiber implementation (e) balance scattering and gradient forces by means of a tightly focused single beam creating a stable 3D trap. Finally, resorting to SLMs, holographic optical tweezers (c) reshape a single beam to create multiple traps.

More recently, seeking additional tunability of the system, wavefront shaping techniques started to be explored for spatial and time manipulation of the trapping potential at the focal plane, see figure 1.1.c. This configuration, commonly called Holographic Optical Tweezers (HOT), involves digital holography techniques achieved by using an active optical element such as a Spatial Light Modulator (SLM), a tunable liquid crystal display that can perform spatial phase modulation. Using specifically computed holograms, multiple traps[21], and dynamical beam steering[22] are two simple examples of the wide range of patterns and applications that can be easily achieved with holographic optical tweezers.

From another perspective, and seeking a more versatile, flexible and on-site solution, fiber optical tweezers (FOT) have recently emerged as surrogates for trapping, while simultaneously being simpler and cheaper[23]. In this configuration, optical forces are induced similarly to the traditional OT setup with the caveat of achieving lower NA. Consequently, gradient forces are generally weaker and trapping becomes harder to realise[23, 24]. To ease this disadvantage, dual counter-propagating fibers configuration such as in figure 1.1.d can be implemented. Alternatively, improved FOT trapping solutions takes advantage of several techniques even allowing trapping with single fiber, see figure 1.1.e. For example, by modifying the fiber tip to form a lens[25] such as tapered fibers, coated or etched tips[26, 27] and modifying the fiber such as multi-mode fibers in holographic optical tweezers configurations[28]

1.2 A brief overview of the applications of Optical Tweezers

These days, OT finds applications in a multitude of areas, from fundamental to applied studies and from research to technological areas. Indeed, since the turning of the century, hundreds of manuscripts have been published each year, making a complete description of the state-of-the-art impracticable for the present document. For this reason, we will restrict to a simplified overview of biological applications, further focusing the scope on the identification and classification of the trapped specimens, which aligns with the purpose of the dissertation. Nevertheless, some good reviews can be found in the literature for other subjects, from which we highlight the following references: cold atoms[29]; quantum physics[30]; chemistry[31].

For biological applications, the first applications report back to the observations of tobacco mosaic virus, *Escherichia coli* bacteria and single-cell trapping[6, 32]. Featuring

no damage above a wavelength threshold and below reasonable beam power[33], optical tweezers emerged then as a revolutionary tool for in vitro and in vivo studies[34, 35] in paths that we can divide into two distinct directions.

On one hand, OT provides a remarkable opportunity for manipulating and playing with biological specimens at the mesoscopic scale. For example, organelle trapping and dragging demonstrate the possibility for micromanipulation within cells[36]. Additionally, random intensity speckles distribute a field of shallow potential wells trapping particles based on their physical properties thus functioning as optical "sieves"[37].

On the other hand, the forces exerted by optical traps conveniently match those of and within biomolecules making OT an exciting opportunity for probing the physical properties of trapped particles. For example, particle-dependent optical trap stiffness, viscosity and diffusion coefficients are measured using a series of methods not only helpful in calibrating an OT setup but also to characterize particles and forces[38, 39]. In different methodologies, transportation by OT was used in the study of extracellular vesicles interaction with cells[40] while the exertion of force permits the study of DNA coiling [41], thermal fluctuations and hydrodynamics of polymers[42], probing cellular[43] and bacterial adhesion[44], just to name a few. Additionally, DNA unravelling around the histone octamer is seen in the quantization of force with elongation when stretching and measuring force [45].

Furthermore, more powerful analysis tools are obtained when combining optical tweezers with other techniques. For example, combining single-molecule fluorescence with optical tweezers allows molecule structure probing such as DNA unbinding[46, 47]. Another powerful combination joins OT and Raman spectroscopy information where the fingerprint characteristic of a spectrum is used to attain accurate particle characterization used for example in the differentiation between live and dead yeast cells[48].

A particularly interesting case study for technological purposes is the identification and classification of trapped particles in the OT, which can be used for optical sorting methodologies. Debuting in 1987, optical sorters used either a single or counter-propagating weakly focused beam setup and an additional probe beam[49]. This setup was capable of sorting particles based on their optical properties by measuring the scattered probe power at 90° and using the optical manipulator to deflect them over distances of millimeters. The advent of this technique began a search for the development of active and passive sorting mechanisms using optical forces to improve upon the simple mechanism implemented.

For example, replacing the intensity probe with an active fluorescence-based identification was observed to achieve fast throughput and high purity sorting[50]. Alternatively, passive particle sorting using optical lattices allows sorting based on size and refractive index with thresholds controlled by particle optical polarizability[51]. Although these methods are successful at sorting particles they present a few caveats in either scalability, time duration or the usage of markers.

In specific, focusing on active classification within the context of optical tweezers, we identify three central methodologies. The first corresponds to an image-based feature search, for example using a camera or speckle analysis of fluorescing or plain cells[52]. Image information treatment uses image processing tools and deep learning algorithms, such as convolution neural networks, which can feature a high throughput during the classification process. Still, the methodology features significant drawbacks, such as the low image quality and the diffraction limit for particles below the micrometer size.

A second technique explores the use of OT integrated with additional Raman spectroscopy information. Its core advantage resides in acquiring a fingerprint signal that can be related to the composition signature. In particular, the Raman spectrum can be analysed with principal component analysis(PCA)[53] and other models[54] to deploy effective particle identifiers. For example, Raman spectra for multi-species classification of single red blood cells were recently reported in the literature[55]. The caveats of using Raman spectroscopy account for the need for an additional excitation laser and longer integration times (up to a few seconds) to improve the signal-to-noise ratio (SNR).

The last methodology mentioned focuses on using the scattered signal to extract input information for a set of machine learning algorithms[15, 56]. The underlying concept is that this signal contains information regarding trapped Brownian dynamics and thus relates to the physical and optical properties of the specimen. This methodology, extensively explored recently by the group of the Center for Applied Photonics at INESC TEC and its spin-off ILOF[56], has the advantage of requiring only cheap and commercially available components and being able to be implemented either in inverted microscope OT or in the more versatile FOT[16]. Still, one of the caveats of the methodology is the relatively high acquisition times, reported to be around 2 seconds for the ILOF technology[56], recently reduced to 500 milliseconds in a recent work[15]. Furthermore, they usually require some pre-processing and feature extraction, which adds significant processing time.

These facts limit the deployment of OT-based ultra-fast classifier solutions, which constitutes the challenge for this dissertation.

1.3 From fast to real-time processing

In the modern age of Big Data, the deep learning (DL) computing paradigm is the state-of-the-art of machine learning, drawing particular emphasis on CNN framework[57]. Generally, ML algorithms require pre-processing and feature extraction to perform a task which implies longer computing routines. In contrast, CNNs require little pre-processing, and feature extraction is intrinsic to the model by optimization of the convolution filter (or kernels) through automated learning, whereas in conventional algorithms these filters are hand-engineered. This independence from prior knowledge and human intervention in feature extraction is a major advantage. Furthermore, when this procedure is made parallel and takes advantage of graphic processor units (GPU) for image processing, CNNs achieve extraordinarily fast performances, which we will be exploring in later chapters. Nevertheless, CNNs require batches of information stored in the machine thus requiring long acquisition times and slow memory systems.

True real-time execution of a computational task occurs when input data is fed continuously to an algorithm thus circumventing pre-processing and feature extraction steps and resulting in almost immediate answers. Evidently, advanced algorithms must be implemented for a task to be performed efficiently and equipped with internal but fading memory[58]. The requirements set for real-time data analysis make it so machine learning algorithms such as CNNs are not suitable to perform this kind of task. Indeed, as they process data in batches, it would require larger memory systems and longer times for data processing. As an alternative neuromorphic architecture, recurrent neural networks (RNN) make use of non-linear and mutable layers whose internal dynamics are governed by input information plus feedback loops, being thus armed with internal memory sub intended in the evolution of the layer states. The caveat of this architecture is the training process of the hidden layer weights, which is often computationally costly and hard to converge[59].

To avoid these difficulties, a new framework within RNN called Reservoir Computing (RC) has recently emerged inspired by biological and analogic data processing[60]. In short, the concept is to replace the hidden layer of RNN with a random, sparse, non-linear, and dynamical reservoir that bypasses the heavy task of training the hidden layer.

Through the nonlinear expansion of the input into a higher dimensional space of states, a nonlinear task can be turned into a linear one without applying pre-processing or feature extraction algorithms[61], thus setting the field for real-time processing as long as the deployed RC algorithm is sufficiently fast.

Additionally, as it requires only a nonlinear reservoir, RC is a suitable framework to bridge from software to actual hardware solutions, spanning across a plethora of supporting physical systems[62]. Of particular interest is the case of optical implementations, that promise fast and parallel computation exploring the native properties of light itself[63]. For example, a simple system such as a Mach Zehnder interferometer intensity modulation together with a delay in a fiber spool can work as a many-node reservoir that is capable of solving digit recognition and non-linear equalization problems[64]. Additionally, using semiconductor optical amplifiers the upper part of the commonly used hyperbolic tangent is approximated resulting in the typically used RC models[65].

1.4 Thesis Outline

The major goal of this dissertation is to explore state-of-the-art algorithms and technological solutions for faster OT-based classification solutions. For that, and within the context described in the last sections, we will first explore the deployment of algorithms based on CNNs, before trying to move towards real-time processing using RC paradigm.

The structure of this dissertation divides into six chapters as follows. First, in **chapter 1** we provide a contextual introduction to historical notes on OT and an overview of its applications for biological purposes, before focusing on the challenges of fast and real-time classification of trapped particles, setting the motivation for the project.

Then, in **chapter 2**, we introduce the basic concepts of OT, providing a theoretical framework for the description of the 3D optical trap and building the necessary connections to understand how optical harmonic traps are shaped. We end this chapter by making the connection to the experimental work, describing the OT setup and experimental procedure used in the data acquisition in this work.

From experimental setup to developing a digital twin, in **chapter 3** we study the Langevin representation of Brownian motion in a harmonic trap together with the overdamped approximation and a brief overview of its statistics and limitations. Lastly, we describe the implementation of an integrator of the overdamped Langevin equation and provide a simple test to verify convergence.

The first interaction with machine learning occurs in **chapter 4** with an introduction to basic concepts required to understand commonly implemented test procedures and interpretation of final results. Then, we present the preparation of the input data to a Convolution Neural Network for the classification of trapped particles. To conclude the chapter we present the results, on experimental or synthetic data, where particles are identified with basis on their size or composition.

The journey toward the real-time classification of optically trapped particles starts in **chapter 5** with the study of recurrent neural networks, particularly the echo state network (ESN) framework. The implementation of an ESN algorithm is discussed and constructed in python being tested for the classification of optically trapped particles in the concluding section.

Finally, in **chapter 6**, we present the concluding remarks and prospective work, mainly focused on the expedition towards real-time optical computing for optical tweezers analysis.

1.5 Original Contributions

Along with the completed work listed below, an article is currently being prepared for submission.

Conference Peer-Reviewed Proceedings:

- **V. Rocha**, J. Oliveira, A. Guerreiro, P. A. S Jorge, and N. A. Silva, "Intelligent Optical Tweezers with deep neural network classifiers", EOSAM Conference Proceedings, 2022.

- J. Oliveira, **V. Rocha**, A. Guerreiro, P. A. S Jorge, and N. A. Silva, "Automation strategies and machine learning algorithms towards real-time identification of optically trapped particles", EOSAM Conference Proceedings, 2022.

- J. Teixeira, **V. Rocha**, J. Oliveira, P. A. S. Jorge, and N. A. Silva, "Towards real-time identification of trapped particles with UMAP-based classifiers", AOP Conference Proceedings, 2022.

- F. Coutinho, J. Teixeira, **V. Rocha**, J. Oliveira, P. A. S. Jorge, and N. A. Silva, "Autonomous Optical Tweezers: from automatic trapping to single particle analysis", AOP Conference Proceedings, 2022.

Oral Presentations

- J. Oliveira, **V. Rocha**, N. A. Silva, P. A. S. Jorge, "Optical Tweezers development as a tool for biomedical diagnosis", Investigação Jovem da U. Porto, 2022.
- J. Oliveira, **V. Rocha**, N. A. Silva, P. A. S. Jorge, "Optical Tweezers development as a tool for biomedical diagnosis", Física 2022.
- J. Oliveira, **V. Rocha**, N. A. Silva, P. A. S. Jorge, "Automation strategies and machine learning algorithms towards real-time identification of optically trapped particles", EOSAM, 2022.

Poster Presentations:

- **V. Rocha**, J. Oliveira, A. Guerreiro, P. A. S. Jorge, and N. A. Silva, "Deep-learning approach to classification of optically trapped particles", Investigação Jovem da U. Porto, 2022.
- **V. Rocha**, J. Oliveira, A. Guerreiro, P. A. S. Jorge, and N. A. Silva, "Recurrent Neural Network classification of optically trapped particles", Física, 2022.
- **V. Rocha**, J. Oliveira, A. Guerreiro, P. A. S. Jorge, and N. A. Silva, "Convolution Neural Network classification of optically trapped particles", EOSAM, 2022.
- J. Teixeira, **V. Rocha**, J. Oliveira, P. A. S. Jorge, and N. A. Silva, "Towards real-time identification of trapped particles with UMAP-based classifiers", AOP, 2022.
- F. Coutinho, J. Teixeira, **V. Rocha**, J. Oliveira, P. A. S. Jorge, and N. A. Silva, "Autonomous Optical Tweezers: from automatic trapping to single particle analysis", AOP, 2022.

Outside of the scope of this work:
Peer-reviewed manuscripts

- T. D. Ferreira, **V. Rocha**, D. Silva, A. Guerreiro, N. A. Silva, "Towards the experimental observation of turbulent regimes and the associated energy cascades with paraxial fluids of light", September 2022, New Journal of Physics.

Oral Presentations

- T. D. Ferreira, N. A. Silva, D. Silva, **V. Rocha**, C. C. Rosa, and A. Guerreiro. "Using fluids of light in photorefractive media to create turbulent states", FÍSICA 2022 – 23ª Conferência Nacional de Física e 32º Encontro Ibérico para o Ensino da Física, Porto, September, 2022.

- T. D. Ferreira, N. A. Silva, D. Silva, **V. Rocha**, C. C. Rosa, and A. Guerreiro. "Experimental turbulent states with paraxial fluids of light in photorefractive media", V International Conference on Applications of Optics and Photonics, Guimarães, July, 2022.

Chapter 2

Fundamentals of Optical Trapping: from theory to the laboratory

This chapter is dedicated to a brief overview of the working principles of OT and of the experimental setup used throughout this work. Starting by understanding OT, we review the two common regimes typically used in the literature for the introduction of physical phenomena. Although these regimes do not provide a complete description of OT, they still give a good picture of the principles behind the trapping of mesoscopic scale particles. Supported by the fundamental concepts of OT, we then discuss the trapping conditions and introduce the simplified harmonic potential approximation that accurately describes single particle manipulation using a Gaussian-shaped beam profile. Finally, we present the experimental OT setup used throughout this thesis, as well as discuss the methodologies and acquisition instruments for the measurement of the position time series.

2.1 Balancing Optical Forces

Optical forces that sustain the trapping mechanism result from the transfer of momentum from the optical trapping beam to the particle.Yet, this mechanical process has distinct physical roots depending on the size of the particle, which is an essential parameter to portray an accurate description of the light-matter interaction. The first regime explains the forces when the particle size (a) is much smaller than the wavelength of light $(\lambda,\ a \ll \lambda)$ and the particle is treated as a point-like electric dipole[66]. In the opposite condition $(a \gg \lambda)$ the regime can be treated using geometric optics[67]. Finally, both models fail to describe the trapping forces for a third intermediate regime $(a \approx \lambda)$, thus requiring a

full electromagnetic description[29]. For the sake of simplicity, we will proceed by focusing our analysis only on the first two regimes, discussing qualitatively the origin of the optical forces and the theoretical framework that may come into play. Furthermore, we simplify the following models by assuming spherical particles. The analysis becomes complex when deformation is added to the particles, meaning that computational simulations become key in studying its effects [68, 69].

2.1.1 Rayleigh approximation

As stated before, the first regime considers particles with sizes much smaller than the wavelength of light ($a \ll \lambda$). In this condition, the particle can be approximated by a dipole (closely related to the so called dipole approximation in quantum optics) induced by the incident electric field. The optical forces can then be easily described by the interaction of this dipole with the electric field.

On one hand, the absorption and re-emission of photons and the associated momentum conservation result in an effective scattering force along the optical propagation direction, which is proportional to the intensity incident on the cross section area σ as

$$F_{scat} = \frac{n_m}{c}\sigma I_0, \tag{2.1}$$

where n_m is the refractive index of the medium and I_0 is the intensity of the incident light. It can be shown[29, 66] that for spherical particles the effective cross-section can be modeled as

$$\sigma = \frac{128\pi^5 a^6}{3\lambda^4}\left(\frac{m^2-1}{m^2+2}\right)^2, \tag{2.2}$$

where m is the ratio between the particle refractive index and that of the optical medium.

On the other hand, a second force component called gradient force arises from the dipole moment interaction with the inhomogeneous electric field, being given by

$$F_{grad} = \frac{2\pi\alpha}{cn_m^2}\nabla I_0, \tag{2.3}$$

where

$$\alpha = n_m^2 a^3\left(\frac{m^2-1}{m^2+2}\right) \tag{2.4}$$

is the particle Clausius-Mossotti polarizability [70]. The gradient force is thus proportional to the intensity gradient. From the Clausius-Mossotti relation, the polarizability can either take negative or positive values depending on the ratio m, making the force

attractive or repulsive in relation to the higher intensity spots, *e.g.* the beam focal point. Indeed, if the particle refractive index is superior to that of the medium we have positive polarizability and therefore a gradient force attracting the particle towards the beam focus; conversely, for particle refractive index inferior to that of the medium, we have a repulsive force.

2.1.2 Ray optics regime

For larger particles, the electric dipole approximation breaks and one should pursue a distinct theoretical framework to understand the physical concepts underlying the trapping phenomena. In particular, when the particle is significantly larger than the wavelength of light, it can be explained using a ray optics formalism.

In the geometric optics (GO) regime, the trapping beam can be visualized as a collection of rays composed of a stream of momentum-carrying photons[71]. By considering a symmetrical beam, an efficient picture is described by opposing pairs of rays resulting in trapping along the axis. Additionally, from the spherical particle assumption, the incident rays and subsequent reflections and refractions can be analyzed over a single plane, as depicted in figure 2.1.

The optical forces arise from the transfer of momentum between the trapping beam and particle resulting from the change in the wavevector magnitude and direction upon reflection or refraction. Along the trajectory of a ray, many reflections and refractions occur that become progressively less relevant[71], but we can limit the description to the first reflection and refraction as contributions from subsequent ones are described analogously. One way to calculate the momentum carried by a single ray is to think of it as a stream of photons each carrying momentum

$$\mathbf{p} = n_i \frac{h\nu}{c}, \tag{2.5}$$

where h is Planck's constant, ν the frequency of the photons, n_i the refractive index of the medium and c the speed of light. In total, a ray's total momentum is given by the sum of contributions from the total number of photons N as

$$\mathbf{P} = N\mathbf{p} = N n_i \frac{h\nu}{c}. \tag{2.6}$$

For a single ray, the force can thus be computed as the contribution of the three terms [71] as

$$F_{ray} = \frac{n_i P_i}{c}\hat{\mathbf{r}}_i - \frac{n_i P_r}{c}\hat{\mathbf{r}}_r - \frac{n_t P_t}{c}\hat{\mathbf{r}}_t, \tag{2.7}$$

where P is the power of the ray and the indexes i, r and t identify the incident, reflected and transmitted light, respectively.

In the following qualitative analysis, we elucidate three trapping situations illustrated in figure 2.1. In general, when a particle's surface deflects a ray, its momentum changes in both direction and magnitude, with a balance in momentum occurring as a result of force applied to the particle. With this in mind, in the first case (a) the trapped particle is dislocated along the axis below the focal point where reflection generates the scattering force (F_{scat}, blue arrows) pushing the particle away from the focal point while refraction induces a gradient force (F_{grad}, orange arrows) restoring the particle towards the focal point. Case (b) describes the complementary situation of a particle above the focal point where both scattering and gradient force contribute to restoring the particle to the equilibrium position. The last case (c) depicts the off-axis situation where the scattering force pushes the particle away from the focal points while the gradient force restores the particle to it.

The previously discussed examples all share the gradient force pulling the particle towards the focus while scattering force pushes it away. Hence, the gradient force must counterbalance the scattering force for 3D optical trapping to be effective. The usual designation of a tightly focused single beam trap results from the fact that this is achieved by ray angles steeper toward the center such as those obtained by tightly focusing the beam.

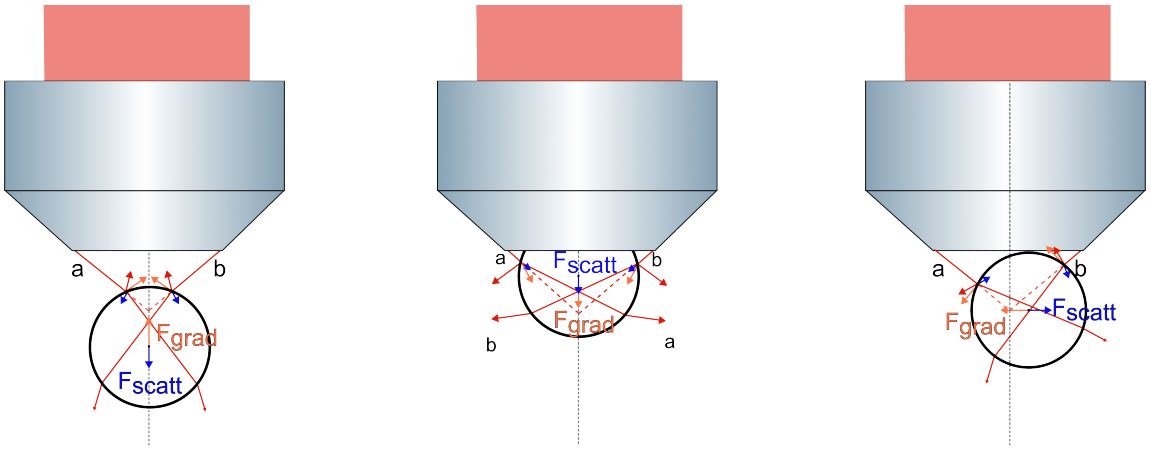

FIGURE 2.1: Illustration of the ray-induced forces on the trapped particle for three distinct situations: (a) below the focus, (b) above the focus and (c) dislocated along the transversal plane.

2.1.3 An effective model for a single-beam gaussian optical trap

While these two regimes are described by totally distinct phenomenology, we note that both descriptions result in two major optical forces of similar effect. On the one hand, we have the scattering force that pushes the particle along the direction of the beam, thus opposing optical trapping needing to be counter-balanced. On the other, the gradient force creates a stable equilibrium point in the highest intensity regions, i.e. focus. Thus, the gradient force must exceed the scattering force for an equilibrium to be created, a condition that strongly depends on the particle size and medium but that is typically achieved only when using highly focused beams. Furthermore, due to the scattering force pushing the particle downwards (along the beam direction), the trap equilibrium position is slightly below the focal point.

To conclude the theoretical discussion of optical trapping we must relate the beams profile with the optical force felt by the trapped particle. Assuming a single Gaussian-shaped beam profile and small displacements around the equilibrium, the trapping potential can be approximated by a harmonic trap and the force given by the Hooke law [29, 71]

$$\mathbf{F} = -\mathbf{k} \odot \mathbf{r}, \tag{2.8}$$

where $\mathbf{k}$ is the stiffness vector and $\mathbf{r}$ the position relative to the equilibrium point. This model strongly simplifies the analysis and provides a suitable and well-established mathematical background to treat optically trapped particles.

2.2 Experimental Setup

So far we have established a theoretical framework and some of the prerequisites for a successful single beam optical trapping. In this section, we bridge theory to the laboratory and present our experimental setup.

The setup used for the experimental work on this dissertation is adapted from the commercial Optical Tweezers (OTKB - Modular Optical Tweezers System, Thorlabs, USA), shown in figure 2.2 and schematically depicted in figure 2.3.

A continuous-wave (CW) 976nm fiber laser diode (Lumentum s27-7602-460) is used for trapping single particles with power emission at 68mW and coupled to a 980nm single mode optical fiber for spatial mode filtering purposes. The choice of the long wavelength seeks to minimize the necessary power which is fundamental for non-damaging trapping

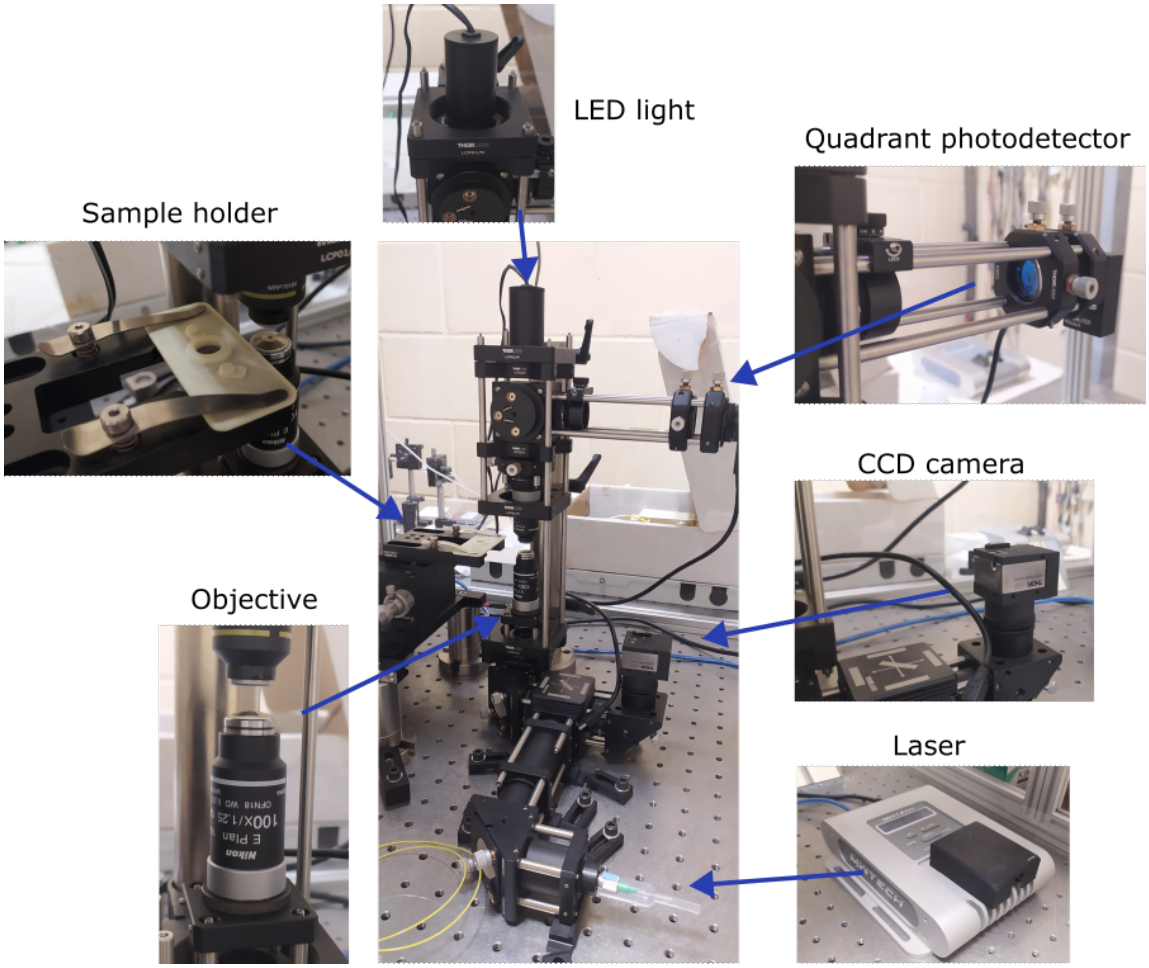

FIGURE 2.2: Inverted microscope objective configuration of optical tweezers used in the experimental component of this work.

procedures. After collimating the beam at the exit of the fiber, a Galilean expander - composed of achromatic doublets of $-50mm$ and $150mm$ focal lengths - is used to expand the beam and completely fill the aperture of the inverted microscope objective, thus maximizing the intensity gradient and inducing stronger gradient forces. For focusing purposes, we used a high numerical aperture (CFI E Plan Achromat $100\times$ Oil) which both matches the necessary gradient conditions for particles in the range of a few micrometers, as well as provides better image resolutions. To cope with such high numerical apertures and minimize refraction and reflection of light in-between surfaces, an immersion oil with refractive index $n_e = 1.518$ at $23°C$ (Olympus IMMIOL - F30CC) is also used. The focus is then used to trap the particles in the sample, which is mounted in a 3-axis positioning stage for scanning the sample as needed.

In this type of setup, called inverted microscope, the objective has both the function of focusing the beam and imaging the particle to a CMOS camera illuminated by a LED.

Thus, an additional imaging arm features a camera (DCC1240, Thorlabs) that captures colour images with a 200mm focal length achromatic lens to image the sample plane at 1280 $\times$ 1024 resolution. To avoid saturation from backscattered light, a shortpass filter with a cut-off wavelength at 750nm is placed before reaching the camera sensor.

Finally and above the sample, we find an arm with a 10$\times$ air condenser lens (E Plan Achromat 10X, Nikon) that collects the beam that is then directed and focused on the photon quadrant detector. For that, we use a neutral density filter OD= 0.6 to avoid saturation and a 40mm lens to focus the beam in the sensor. The photon quadrant detector (PDQ80A, Thorlabs) operates for a wavelength range between 400 $-$ 1050nm and is capable of 150kHz bandwidth. For the purposes of this work, it is set to a sampling rate of 10kHz, sufficient to track the particle motion while maximizing the signal-to-noise ratio.

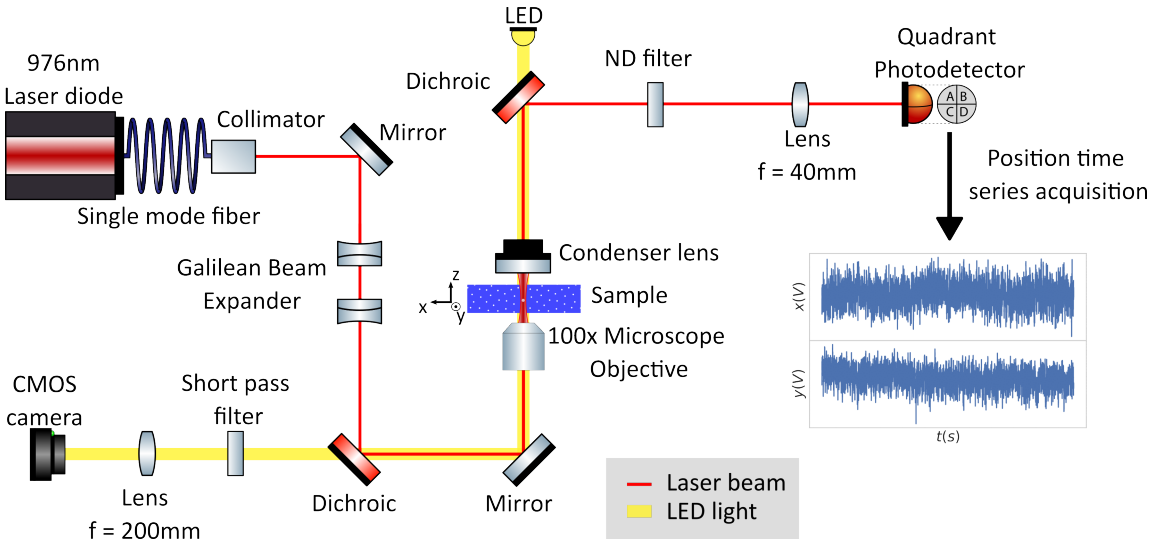

FIGURE 2.3: Schematics of the inverted microscope configuration featuring a photon quadrant photodetector for the acquisition of the forward-scattered signal.

2.2.1 Tracking the position of the particle

Tracking the particle motion precisely is an essential requirement for particle characterization in the context of OT. In the particular case of our setup, we explore the concept of laser-based position detection. Summarizing, while the inverted microscope focuses the beam in the plane of the particle, the condenser collects the forward scattered light that, imaged in the Fourier space using the 40mm lens in the back focal plane of the condenser, can provide information of the position using the quadrant photodetector.

The photon quadrant detector is a semiconductor silicon photodiode divided into four sections (quadrants), see figure 2.4. By imaging onto the quadrant photodetector the

transmitted beam from the trapped particle, a change in the particle position induces a beam deflection measurable as a differential of the intensities of each quadrant. From each quadrant intensity, the position of the beam relative to a reference can be obtained via the formulas

$$\begin{aligned} X &= \frac{(Q_2 + Q_3) - (Q_1 + Q_4)}{Q_1 + Q_2 + Q_3 + Q_4} \\ Y &= \frac{(Q_1 + Q_2) - (Q_3 + Q_4)}{Q_1 + Q_2 + Q_3 + Q_4}, \end{aligned} \tag{2.9}$$

where Q_1, Q_2, Q_3 and Q_4 are the quadrant intensities. The denominator is the total intensity, usually denominated as SUM, which accounts for intensity fluctuations. From the experimental perspective, the reference point is obtained by setting the differences to zero when the laser crosses the system without any obstacles, i.e. the beam is centered.

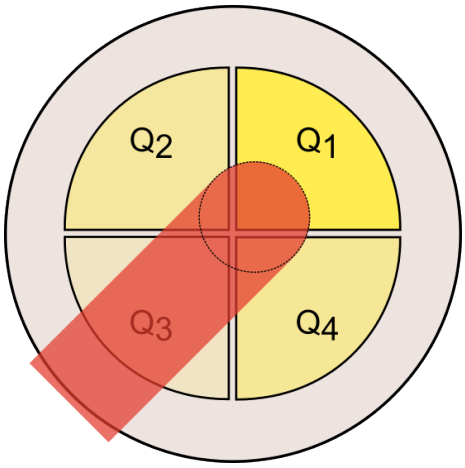

FIGURE 2.4: Illustration of the quadrant photodetector where deflections of the beam induced by particle displacements are detected by the quadrants.

Assuming a linear relation between the beam position in the QPD and the particle position, the absolute position can also be acquired using a conversion factor. The conversion factor depends on the beam parameters and for our setup it was previously obtained in reference [72].

To conclude this section a short comment must be made on the relation between the SUM values and longitudinal direction (z). Technically, the longitudinal direction is encoded in the SUM values. Yet, this dependence is non-linear and hard to characterize. Due to these reasons, throughout this work, we will not be making use of the SUM value. Nevertheless, the methodologies deployed will be general enough to include this additional source in the future, provided solid theoretical and experimental knowledge is developed beforehand.

2.2.2 Experimental procedure

To ensure good and reproducible results, and avoid unwanted experimental bias in the data, we devised a protocol for data acquisition.

The implemented protocol requires a micro-pipette $1 - 10\mu L$ (e.g. P10 model, GILSON) and a pipette $100 - 1000\mu L$ (e.g. P1000 model, GILSON), plus distilled water and a glass beaker. For each experiment (i.e. for each class of particles) the following set of consumables are necessary: pipette tips (compatible with each pipette), an eppendorf, and a plastic pipette. Sample preparation for each type of particle was made with an eppendorf for each class to avoid mixing of particles and allow us to keep track of the particle labels.

To prepare each sample, we began by placing enough distilled water in the glass beaker to later withdraw $2mL$ using a pipette with an unused tip. Then, we place the pipette content in the eppendorf where the sample is to be prepared, and using the smaller pipette with a new tip we withdraw from the container $1\mu L$ of particle in preparation. The tip of the pipette is submerged in distilled water to dilute the particles. Then, we clean the pipette from any remaining particles by withdrawing some solution and placing it back in the medium. The solution comes to a concentration of 0.05%. This small concentration is used to avoid particle interaction during data acquisition. Finally, we remove the pipette and close the eppendorf. The tips from the pipettes shall be discarded responsibly to avoid cross-contamination issues.

For the acquisition process, a small sample withdrawn from the eppendorf using a plastic pipette (three drops are used) is placed in the sample holder (figure 2.2). A drop of the aforementioned oil is placed on the microscope objective and the sample holder is then placed on the positioning stage and lowered until the oil fills the gap between the objective and the sample holder. In order to avoid measuring the same particle twice - thus creating a bias in the experimental data set - we measure a single particle from each sample withdrawn from the eppendorf. After trapping, each acquisition of the position time series lasts around 20 seconds, but we shall stress that the low concentration of the sample makes it hard to find a single particle, which means that a single measurement process is very slow and can take between $5 - 15$ minutes for a single particle. Finally, we shall also note that we must randomly iterate between classes of particles and samples throughout the whole experimental period to assure that changes in experimental conditions (e.g. temperature variation throughout a day) do not introduce unwanted data bias.

2.3 Concluding remarks

In this chapter, we reviewed the theoretical background to support the interpretation of the optical trapping phenomena using a single tightly focused beam. Furthermore, by taking into consideration the relation of optical gradient force with the intensity gradient in the beam transverse plane, we introduced an effective harmonic model that is valid for small displacement and gaussian-shaped traps, the typical experimental conditions that we explore in this dissertation and feature in our experimental setup.

Then, we presented the optical tweezers setup we used for the trapping and signal acquisition procedures. We explained the working principles and the mechanism for relating the information acquired from the forward scattered beam using a quadrant photodetector with the position of the particle. Also, we discussed the reasons for which we will discard the longitudinal position information from further analysis, arguing that the conversion between intensity measurement and position is complex to model and strongly dependent on the setup conditions, introducing possibly unreliable information that can be detrimental to our purposes.

To conclude the chapter, we described an experimental procedure that we have designed and used for creating the experimental datasets, making the procedure reproducible and less susceptible to unwanted bias from variable experimental conditions. This is also an important step to account for class representation as required by machine learning applications.

Chapter 3

Developing a digital twin

As we saw before, when a particle immersed in a medium is optically trapped, there is a balance between two optical forces that can be translated into an effective harmonic model for the single gaussian-shaped beam. However, there are still additional effects that must be taken into account, in particular the viscosity of the medium and the stochastic processes brought on by nearby particle collisions.

In this chapter, we introduce a mathematical model for this Brownian-like motion by means of the overdamped Langevin stochastic differential equation, in an attempt to develop a digital twin capable of simulating the acquired signal to validate our experimental results and methodologies. We discuss some common techniques for the study of such stochastic processes, including probability distribution and mean square displacement. Based on these concepts, we present three common calibration methods of OT that can allow the determination of the particle-dependent physical properties of the particle to fine-tune our digital twin model to match the experimental results. To conclude, we described the implementation of a simulator for the overdamped Langevin equation and provide a simple test of the simulator to verify the convergence of the statistical properties of the simulation with the theoretical predictions.

3.1 A Langevin model for the trapped particle

When immersed in a medium, the dynamics of an optically trapped particle result from an interplay between stochastic Brownian motion, optically induced Hook-like forces and viscous drag, see figure 3.1. This results in a random walk that can be described in terms of a stochastic differential equation named the Langevin equation[71, 73, 74]. Taking the

harmonic oscillator model from the previous chapter, the Langevin model reads

$$m\frac{d^2}{dt^2}\mathbf{r}(t) + \gamma\frac{d}{dt}\mathbf{r}(t) + \mathbf{k}\odot\mathbf{r}(t) = \gamma\sqrt{2D}\boldsymbol{\chi}(t), \tag{3.1}$$

where m is the particle mass, γ is the viscosity, D is the diffusion coefficient and $\odot$ represents the element-wise product. On the left side, we have the position-dependent quantities. The first term is the inertia of the particle, which is not present in the original Einstein model for the Brownian motion. The inertia of the particle is particularly significant for smaller time scales or heavier particles where the ballistic behaviour becomes relevant. The second term is the dissipation emerging from the friction between the particle and the surrounding fluid i.e. the viscosity. The last term on the left side is the trapping Hook-like force induced by a Gaussian-shaped beam.

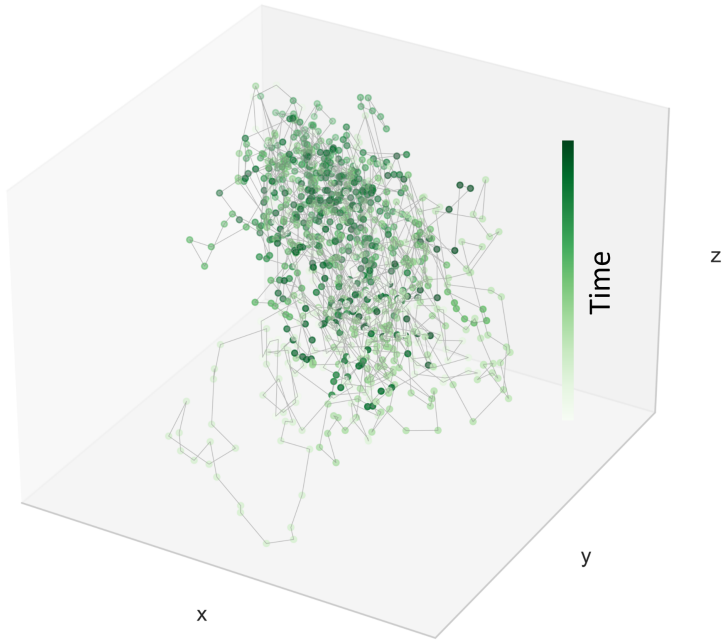

FIGURE 3.1: Illustration of an experimentally trapped random walk of a $3\mu m$ Polystyrene particle resulting from an interplay between Brownian motion, light-induced forces and viscous drag.

On the right-hand side, we have a stochastic vector term $\boldsymbol{\chi}(t)$ that accounts for the interactions between the particle and the surrounding fluid. One of the properties of this term is that, as in the Einstein model, it allows to establish the diffusion coefficient. In the Langevin equation, this is warranted by setting the stochastic term distribution as the solution of the diffusion equation [75]. Thus, by including the factor $\sqrt{2D}$ in equation

3.1 we are implicitly saying that the term $\boldsymbol{\chi}(t)$ has unity variance. Also, the white noise nature of the stochastic term means that it must feature[71, 74, 76]

- $\langle \boldsymbol{\chi}(t) \rangle = \mathbf{0}$, and
- $\langle \boldsymbol{\chi}(t_1) \odot \boldsymbol{\chi}(t_2) \rangle = \boldsymbol{\delta}(t_1 - t_2)$,

where the average is taken over many ensembles. In short, the first property states the zero mean for the distribution, while the second implies zero correlation between two values when evaluated at different times.

A common approximation that is used in OT is neglecting the inertial term, which is usually smaller than the dissipation induced by viscous drag ($\tau_m = m/\gamma \to 0$) and the collisions term. By neglecting the inertial term the particle dynamics can be modelled by the overdamped Langevin equation [71]

$$\frac{d}{dt}\mathbf{r}(t) + \frac{\mathbf{k}}{\gamma} \odot \mathbf{r}(t) = \sqrt{2D}\boldsymbol{\chi}(t), \tag{3.2}$$

which is simpler to explore mathematically and easy to simulate computationally. Naturally, by removing the inertial term this model accounts only for the diffusive behaviour of the particle. Thus, we shall note that by not accounting for the inertia of the fluid this model fails to accurately describe the particle dynamics for very small time scales or larger particles[74, 77, 78]. Nevertheless, the time scales used in this work are sufficiently large to consider this simplified inertia-less regime an accurate description of the trapped Brownian-like motion.

3.2 Statistical properties and distributions

While the process is inherently stochastic, one can still access particle properties and dynamical parameters by studying the statistical quantities of the position time series. Indeed, using the overdamped Langevin model, we can easily deduce a series of expressions describing the relations between physical and statistical quantities. We are mainly interested in the relations portraying the probability distributions, i.e. the distribution moments.

Starting with the position density distribution, thermalization of the trapped particle with the neighbouring fluid constituents results in the well-known Boltzmann distribution where the energy is approximated by the optically-induced harmonic trap[39]

$$\rho_i = \frac{k_i}{2\pi k_B T}^{-\frac{1}{2}\frac{r_i^2}{k_B T/k_i}}, \tag{3.3}$$

where k_B is the Boltzmann constant, T the temperature of the system and i indexes the transversal direction (x, y). Proof of this distribution is given in section 3.3 where in figure 3.4 we show the match between the normal distribution and experimental time series histograms.

From equation 3.3, we directly withdraw the variance as

$$\left\langle \left(r_i - r_{eq,i} \right)^2 \right\rangle = \frac{D\gamma}{k_i} = D\tau_{ot,i}\,, \tag{3.4}$$

where the Stokes-Einstein relation, $D\gamma = k_B T$, was used to relate the thermal energy with the physical properties of the particle and $\tau_{ot,i} = \gamma/k_i$ is the trap characteristic relaxation time. A caveat of using this position information is that it may be susceptible to the presence of long timescale drifts, for example, originating from residual fluid velocities or convective currents.

One path to bypass this problem is to consider the subtraction of time-delayed positions, minimizing the long-term mean drift effects. This transformation leads us to what is known as displacement, defined as

$$\mathbf{d}\,(t) = \mathbf{r}\,(t) - \mathbf{r}\,(t - \Delta t)\,, \tag{3.5}$$

where Δt is a short time interval between positions. As before, the statistical description for the average displacement is also possible to derive by extending the position model. The density distribution of the displacement, much like the position distribution, is a zero-centered Gaussian with the only non-zero moment being the variance, see figure 3.2. The displacement variance is commonly denominated mean squared displacement (MSD) and is defined as

$$\mathrm{MSD}_i\,(\Delta t) = \left\langle \left[r_i\,(t + \Delta t) - r_i\,(t) \right]^2 \right\rangle, \tag{3.6}$$

where the mean is taken over an ensemble of random walks acquired in a time interval T where $T \gg \tau_{ot}$. Using the formal solution to the overdamped Langevin equation 3.2[39,

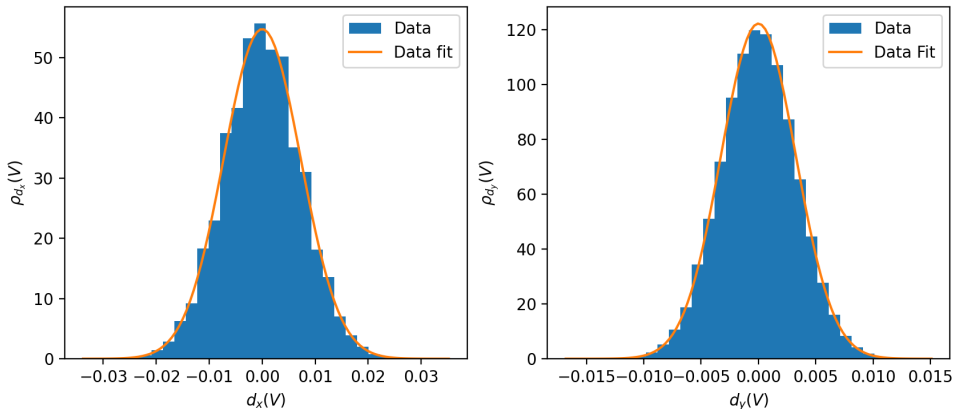

FIGURE 3.2: Displacement distribution of a $3\mu m$ PS particle.

73] as calculated in the appendix A, the MSD is given by

$$\mathrm{MSD}_i\left(\Delta t\right) = 2D\tau_{ot,i}\left(1 - e^{-\frac{\Delta t}{\tau_{ot}}}\right). \tag{3.7}$$

Compared with the position information, displacement representation of the properties of the particle comes altered by a non-linear transformation tuned by the time interval, as seen in figure 3.3.

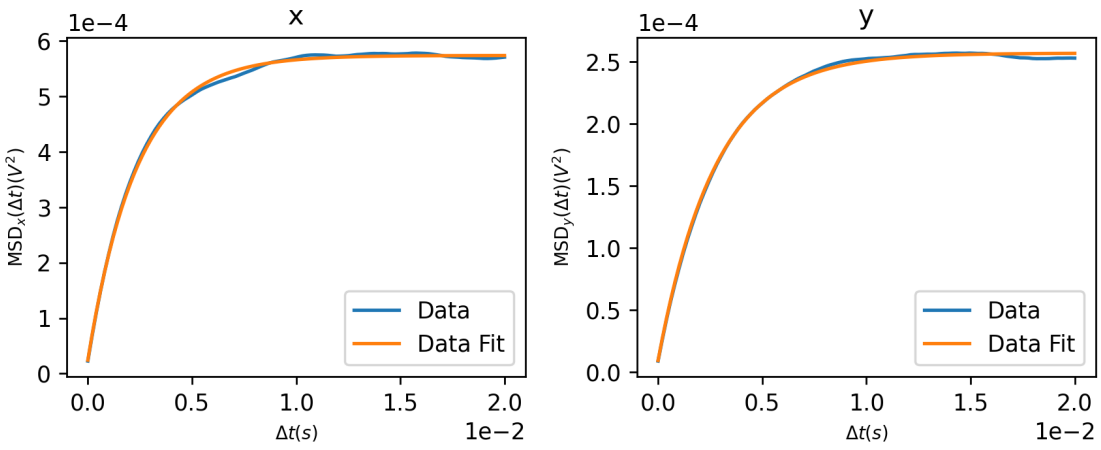

FIGURE 3.3: Dependence of the MSD on the time interval between positions. On the left and right are located the MSD in the x and y directions, respectively. The points are obtained from the experimental position time series of a $3\mu m$ Polystyrene bead, where the MSD is computed by averaging the displacement with fixed time intervals between positions. The points are then fitted to the equation 3.7 in the main text.

3.3 Calibrating the model to the experimental world

Optical tweezers are capable of exerting very small forces of the order of picoNewtons on trapped particles that can be determined using calibration methods. In this section, we review three of the most common and easy calibration methods: potential analysis, equipartition method and power spectral density (PSD). The first two methods make use of the statistics of the particle while the third uses the frequency dynamics of diffusion[39]. As will be seen, the principles used in these methods restrict the physical quantities possible to be obtained using each technique. As an illustration for each of the three methods, figure 3.4 comprises the principles used in each technique.

3.3.1 Potential Analysis Method

Starting with a statistical physics approach, the potential analysis or Boltzmann method makes use of the position density distribution to estimate the optical force of the trap. This restricts the method to measure properties of the trap e.g. trap stiffness $\boldsymbol{k}$ for the harmonic potential case. In general, for a potential field $U(\mathbf{r})$ the position density for a particle in thermal equilibrium with the environment is given by the Boltzmann distribution

$$\rho(\mathbf{r}) = \rho_0 e^{-\frac{U(\mathbf{r})}{k_B T}}, \tag{3.8}$$

where ρ_0 the normalization constant, k_B Boltzmann constant and T is the temperature. As no shape of potential field is assumed beforehand, this model can be used for any trap shape. Furthermore, inverting equation 3.8 allows estimation of the shape and strength of the potential field resulting in

$$U(\mathbf{r}) = -k_b T \ln\left(\frac{\rho(\mathbf{r})}{\rho_0}\right). \tag{3.9}$$

Computationally, this method can be translated to an algorithm as follows:

1. Compute the histogram of each one of the M timeseries (length T) for a well-established range of extreme values to standardize the R bins intervals. Calculate the normalized histogram of the M timeseries ρ_m in this range;

2. Calculate the mean $\rho(\mathbf{r})$ and variance $\Delta\rho(\mathbf{r})^2$ according to

$$\rho(\mathbf{r}) = \frac{1}{M}\sum_m \rho_m(\mathbf{r}) \quad \text{and} \quad \Delta\rho(\mathbf{r})^2 = \frac{1}{M-1}\sum_m \left[\rho_m(\mathbf{r}) - \rho(\mathbf{r})\right]^2; \tag{3.10}$$

3. Finally, estimate the physical parameters by fitting the density to equation 3.8. This step requires defining the shape of the potential field which in our case is the harmonic potential, allowing us to calculate the stiffness $\mathbf{k}$ and the equilibrium position $\mathbf{r}_{eq}$. Alternatively, we can adjust the last step to use equation 3.9 instead.

3.3.2 Equipartition Method

The equipartition method is an extension of the potential analysis for the restrictive case of an harmonic potential. Plugging the harmonic potential,

$$U(\mathbf{r}) = \frac{1}{2}\mathbf{k} \cdot \left(\mathbf{r} - \mathbf{r}_{\text{eq}}\right)^2, \tag{3.11}$$

in equation 3.8 the position distribution given by Boltzmann distribution becomes

$$\rho(\mathbf{r}) = \rho_0 e^{-\frac{k\left(\mathbf{r}-\mathbf{r}_{\text{eq}}\right)^2}{2k_bT}}. \tag{3.12}$$

From this distribution, we immediately get the variance as

$$\langle \left(r_i - r_{i,\text{eq}}\right)^2 \rangle = \frac{k_BT}{k_i}. \tag{3.13}$$

Inverting this equation results in the relation

$$k_i = \frac{k_bT}{\langle \left(r_i - r_{eq,i}\right)^2 \rangle}, \tag{3.14}$$

which is used to obtain the stiffness of the trap from the variance of the position time series. This method allows for a faster determination of the stiffness when compared to the potential analysis as it does not require the fitting of a function. Yet, it does not work for an arbitrary potential shape.

3.3.3 Power spectral density method

The third method we present can be derived directly from the Langevin equation. The derivation of the PSD expression for the Langevin equation is presented in appendix B followed by the overdamped approximation given as

$$\text{PSD}_i(f) = \langle |r_i(f)| \rangle^2 = \frac{1}{2\pi^2}\frac{D}{f_{c,i}^2 + f^2} \tag{3.15}$$

where $r_i\left(f\right)$ is the Fourier transform of the position time series, f is the frequency and $f_{c,i} = \frac{k_i}{2\pi\gamma}$ is the corner frequency. The diffusion coefficient and optical trapping time are estimated through a fitting of the experimental power spectrum.

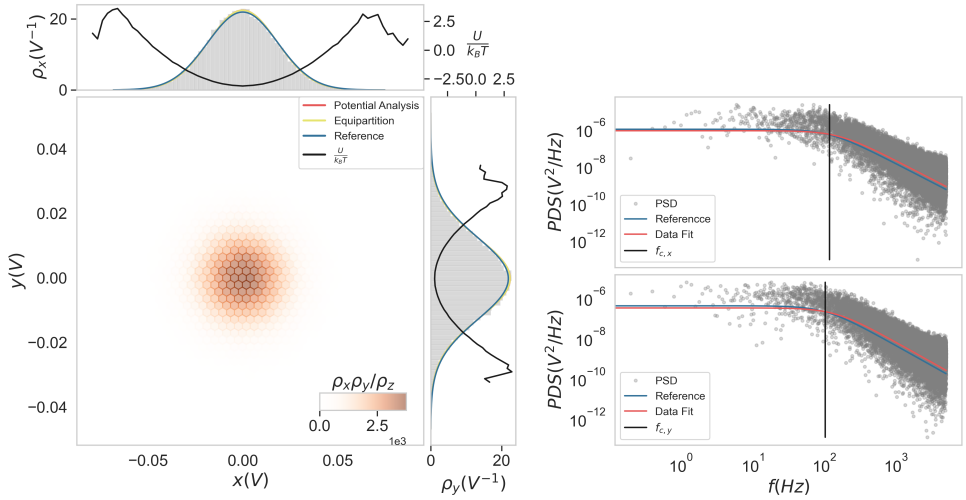

FIGURE 3.4: Visual representation of the potential analysis and equipartition calibration methods (left) making use of the position time series distributions and the PSD method (right) representing both long-term drift and the short-term Brownian dynamical effects which are separated by the corner frequency. The results originated from the experimental position time series of an optically trapped $3\mu m$ Polystyrene particle.

3.4 Implementing a digital twin

Supported by the physical model we have introduced in the last sections and its associated calibration procedures, we are now in conditions to describe the implementation of a digital twin of our experimental setup. The final intent is to support the testing of the classification methodologies we will later explore, as well as validate the experimental results obtained.

3.4.1 Adimensional overdamped Langevin equation

To avoid numerical stiffness and convergence issues, converting the equation into dimensionless units is a helpful and common approach in computational physics. Thus, we begin the digital twin implementation by introducing some easy algebraic manipulations on the overdamped Langevin equation.

To nondimensionalize the Langevin equation we start by introducing time and position transformations

$$\mathbf{r} = r_s \mathbf{r}'; \quad t = t_s t' \tag{3.16}$$

where $\mathbf{r}'$ and t' are our new adimensional variables. Replacing this in the Langevin equation, equation 3.1, results in

$$\frac{m r_s}{t_s^2}\frac{d^2\mathbf{r}'}{dt'^2} + \frac{\gamma r_s}{t_s}\frac{d\mathbf{r}'}{dt'} + r_s k \odot \mathbf{r}' = \frac{\gamma\sqrt{2D}}{\sqrt{t_s}}\chi\left(t'\right), \tag{3.17}$$

where we stress the fact that the stochastic term is inversely proportional to $\sqrt{t}$, thus requiring the additional factor. Taking the overdamped approximation we get the adimensional overdamped Langevin equation as

$$\frac{\mathrm{d}\mathbf{r}}{\mathrm{d}t} + t_s\frac{\mathbf{k}}{\gamma} \odot \mathbf{r} = \sqrt{2D}\frac{\sqrt{t_s}}{r_s}\boldsymbol{\chi}\left(t\right) \tag{3.18}$$

where we dropped the primes for the sake of simplicity. From equation 3.18 we take the hint for the expression of the position scaling coefficient defining it as

$$r_s = \sqrt{2Dt_s}, \tag{3.19}$$

resulting in the expression

$$\frac{\mathrm{d}\mathbf{r}}{\mathrm{d}t} + t_s\frac{\mathbf{k}}{\gamma} \odot \mathbf{r} = \boldsymbol{\chi}\left(t\right). \tag{3.20}$$

In its turn, the time scale coefficient will act as a free parameter for defining a timescale, taking into consideration also the order of magnitude of the stiffness.

To conclude, we must recall the existence of a non-linear transformation of experimental measurements in the longitudinal direction and the position values. The nonlinearity of the transformation forbids a faithful description of the measurements in this direction. Nevertheless, by simulating using adimensional units and considering only the position in the transverse plane, the digital twin is still reliable as long as the overdamped model is valid.

3.4.2 Numerical integration using a fourth-order Runge-Kutta

The numerical integration of the Langevin equation is performed using a standard fourth-order Runge-Kutta (RK4). To implement it, we start by identifying the derivative of the

variable to be integrated as

$$\mathbf{f}(\mathbf{r},t) = -t_s \frac{\mathbf{k}}{\gamma} \odot \mathbf{r} + \chi(t)\,. \tag{3.21}$$

Using this function we calculate the RK4 coefficients dividing each integration step into four contributions as

$$\begin{aligned} \mathbf{K}_1 &= \mathbf{f}(\mathbf{r}, t) \\ \mathbf{K}_2 &= \mathbf{f}(\mathbf{r} + \Delta t K_1/2, t + \Delta t/2) \\ \mathbf{K}_3 &= \mathbf{f}(\mathbf{r} + \Delta t K_2/2, t + \Delta t/2) \\ \mathbf{K}_4 &= \mathbf{f}(\mathbf{r} + \Delta t K_3, t + \Delta t). \end{aligned} \tag{3.22}$$

Before advancing, we must notice a key aspect of the calculation of the RK4 coefficients involving the time-dependent stochastic term. Indeed, the stochastic term is defined at each given time interval. Hence, to keep its characteristics when iterating in time (see figure 3.5), the stochastic term value used in the calculation of simultaneous coefficients must be made with the same stochastic value. Lastly, a simple and natural choice for the distribution from which to draw these random values is the zero-centered normal distribution with unity variance [71, 79].

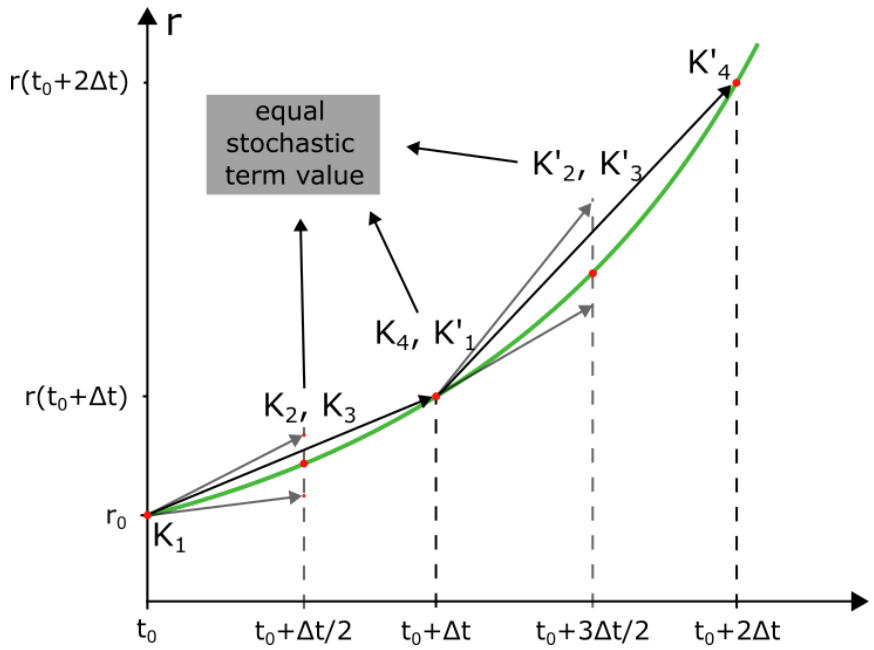

FIGURE 3.5: Visual representation of the RK4 integration method where we call attention to the evaluation of simultaneous coefficients using the same stochastic value.

The numerical integration of the Langevin equation is then simply done by iterating in time the algorithm

$$\mathbf{r}(t+\Delta t) = \mathbf{r}(t) + \frac{\Delta t}{6}\left(\mathbf{K}_1 + 2\mathbf{K}_2 + 2\mathbf{K}_3 + \mathbf{K}_4\right), \tag{3.23}$$

where an initial position $\mathbf{r}(0)$ must be given beforehand.

To conclude the discussion, care must be taken when choosing the time step. As in ordinary differential equations, a good rule of thumb is to choose a time step that is considerably smaller than the smallest characteristic time in the equation. Yet, we should note that the stochastic differential equations the stochastic term depends inversely in $\sqrt{\Delta t}$ and therefore smaller timescales must be avoided as the term diverges for $\Delta t \to 0$ [79].

3.4.3 Code deployment and validation

For deploying our digital twin we implemented the RK4 integrator of the overdamped Langevin equation in Python using the *Numba* package to increase the simulation performance. The code was developed using a modular framework, which allows the user at distinct levels of expertise to explore the simulation tool using the Jupyter notebook workflow. A library with the necessary calibration functions and other auxiliary processing and visualization tools was also created to ease the interpretation of the results.

To validate the model and the tool, we calibrated the digital model to match the particle properties determined from an experimental time series acquired for a $3\mu m$ polystyrene particle using the PSD method to obtain the reference value, as presented in Table 3.1. Introducing these values in the simulator, we simulated 10^6 points with time steps of $10^{-4}s$ resulting in $100s$ time series. The multiple calibration models were then applied to calculate the variance of the synthetic data time series, results presented in table 3.1 and figure 3.6. As can be concluded from the similarity between the data simulated and the reference value, the code converges into a faithful simulation of optically trapped particles.

Axis	$\frac{k_{\text{Reference}}}{k_B T}\left(10^{-4}V\right)$	$\frac{k_{PA}}{k_B T}\left(10^{-4}V\right)$	$\frac{k_{EP}}{k_B T}\left(10^{-4}V\right)$	$\frac{k_{PSD}}{k_B T}\left(10^{-4}V\right)$
x	4.42 ± 0.01	4.13 ± 0.03	4.2 ± 0.1	4.662 ± 0.007
y	2.439 ± 0.005	2.31 ± 0.08	2.29 ± 0.08	2.525 ± 0.003

TABLE 3.1: A good convergence is obtained in the position variance between the reference value used in the simulations (first column) and the outputted by the implementation of the three calibration methods: potential analysis (second column), equipartition methods (third column) and PSD (fourth column). The data is obtained by simulating a $3\mu m$ Polystyrene bead using the developed digital twin.

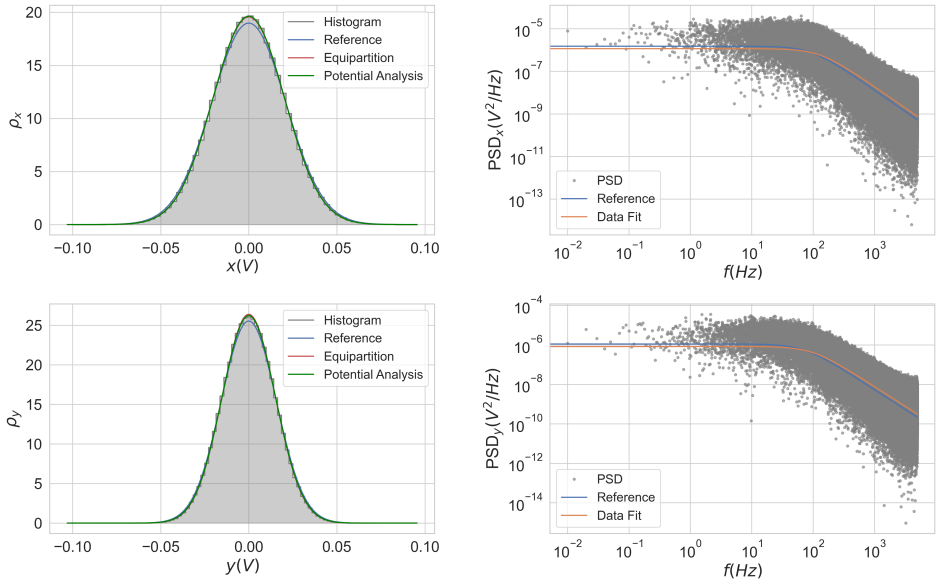

FIGURE 3.6: Application of the potential analysis (green), equipartition method (red) and PSD (orange) to the digital twin simulated time series. We highlight the resemblance between the expected values (blue) of the normal distribution obtained by the potential analysis and equipartition method (left) and the PSD (right).

3.5 Concluding remarks

In this chapter, we modelled the dynamics of a trapped particle as arising from the interplay between the optically induced forces, the stochastic Brownian motion, and the viscous drag using a Langevin equation model. We investigated the model to relate the statistical properties of the position and displacement with the dynamical properties of the particle and medium, namely through the shape and variance of the distributions. We have shown that position and displacement may complement each other information of the system and then act as inputs to a machine learning algorithm.

In a second stage, we shown how to extract from the position time-series the physical parameters that enter in the mathematical model, such as the stiffness, diffusion or relaxation time. From these so-called calibration methods, we presented three of the most commonly used in the OT community: potential analysis, equipartition method and power spectral density.

Finally, using this model and calibration procedures, we described the implementation of a digital twin for our experimental OT setup by the means of a numerical RK4 integrator to solve in time the overdamped Langevin equation. We confirm the solver accuracy

for mimicking the data acquired, establishing thus a valuable tool to help and validate classification algorithms and methodologies as we will explore in the next sections.

Chapter 4

Convolution deep neural network approach to classification of optically trapped particles

As concluded from the previous chapter, optically trapped particles have their physical properties encoded in the position and displacement time series, thus making these rich sources of information to be fed to a machine learning algorithm for classification and identification purposes. In this chapter, we will explore this fact and look at the possibility of using Convolutional Neural Networks to classify the trapped specimen.

With this aim, the chapter begins with a general but brief introduction to a series of concepts in training neural networks (NN), optimization and evaluation of models, and how to visualize and interpret the test results with confusion matrices. Then, by focusing on the specific case of the CNN, we proceed with a discussion of the convenient input data for this machine learning model, describing the process of image creation from the time series, together with the normalization and standardization procedures. Then, after training a CNN, we run a series of tests on particle size and composition classification, comparing with those obtained from the digital twin for validation purposes. We end the chapter with a critical discussion of the results and possible improvements or extensions of the methodology that are ready to be explored in future work.

4.1 A brief note on machine learning and neural networks

In general terms, we can say that machine learning corresponds to a toolbox of computational methods that automatize the process of building analytical models using data analysis. To further refine the discussion, we can also identify three methodologies for the process of training a machine learning algorithm: unsupervised learning, reinforcement learning and supervised learning. The first method is able to perform density estimation, clustering, and dimensionality reduction tasks without prior knowledge of the targets, while reinforcement learning solves any task where decisions can be classified into two classes. Lastly, for the most general purpose such as regression and classification tasks, we commonly use supervised learning, taking both variable and output target labels for the training process. In the present work, we are interested in the classification process for identifying and grouping particles into labelled groups, see figure 4.1.

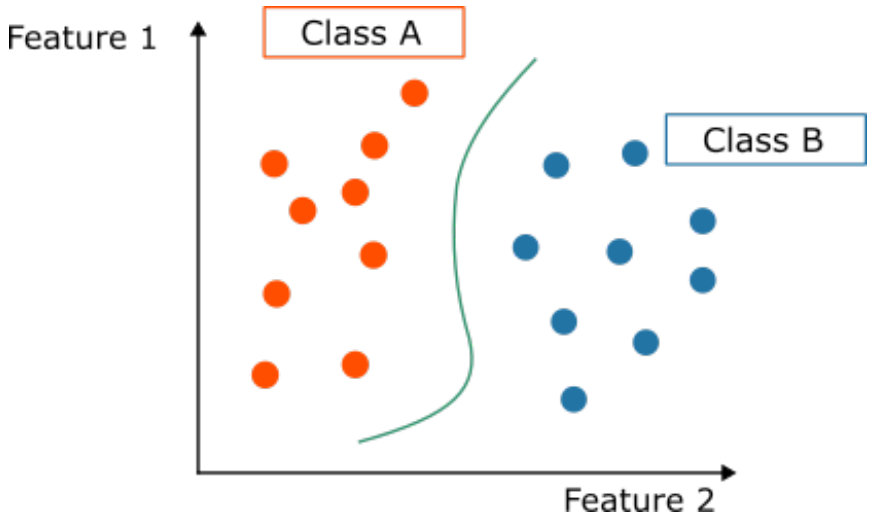

FIGURE 4.1: Illustration of machine learning classification between classes A (orange) and B (blue) where a threshold (green) is developed during supervised training.

Within the supervised learning methodologies, neural networks assumed in the last decade a prominent position in the many classes of machine learning algorithms for scientific purposes. Spite being around for many years, these neuromorphic-inspired methods benefited from the recent development of the GPU industry, making use of this specialized hardware to process large volumes of data and models of many degrees of freedom in a timely manner. To understand its inner workings, one can take the example of the single-layer neural network, mathematically represented by

$$y_{output} = f\left(\mathbf{W} \cdot \mathbf{X}\right), \tag{4.1}$$

where **W** is the hidden layer weight matrix, **X** is the input information and f is a non-linear function named activation function. A layer is composed of a number of nodes, each represented by a row of the weight matrix that intakes the information and projects accordingly to the values of each node weights. The treatment of a single-layered neural network is the same as deep neural networks, with the latter having added complexity due to consecutively stacked layers.

The training of a neural network in supervised learning then consists of optimizing the layer weights that minimize the loss function reporting the distance between output and expected label. A common method to search for local and global minimums of the loss function is to apply back-propagation techniques together with gradient descent methods[80]. In short, this method back-propagates the loss value and derivatives that indicate in which direction each weight must go in order to lower the loss function. Since we will use this training method, it is important to mention that we can define a learning rate hyperparameter l_r that controls the weight update magnitude. In figure 4.2 we illustrate three cases to take into account when choosing l_r. In the first case, the l_r is too high making the loss value jump over the minimum and can even move out of the well. In the second case, the l_r is too small, resulting in slow convergence to the minimum and requiring more train time. Finally, a good value of l_r is found resulting in both good and fast convergence.

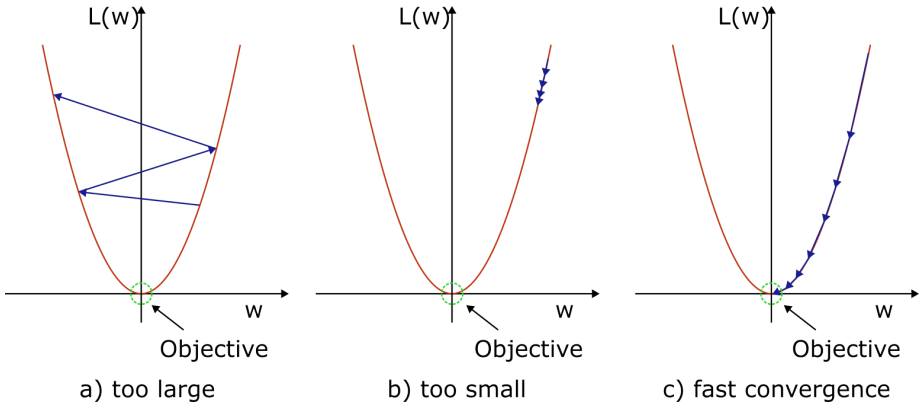

FIGURE 4.2: Gradient descent method for minimizing the loss function with (a) large l_r where algorithm diverges from the minimum, (b) small rate resulting in slow convergence and (c) optimal value which results in good and fast convergence.

In classification problems where each example is restricted to belong to a single class, the labels are encoded into a vector of probability distributions reflecting the likelihood of an example belonging to a given class. In other words, the vectors representing labels are zero except in the entry associated with the true class of the example where a one

indicates the certainty of the class, see figure 4.3. In a neural network algorithm, the classification outputs a vector of likelihoods representing the confidence that the example belongs to each class. From these, we extract the predictions by taking the index with the highest likelihood. Furthermore, this representation allows the use of the categorical cross-entropy loss function, given by

$$L(y_{\text{label}}, y_{\text{predicted}}) = -log\left(\frac{p_t}{\sum_{i\in\{\text{classes}\}} e^{p_i}}\right) \tag{4.2}$$

where p_i is the index i of the output vector of probabilities and p_t is the probability of the true label. In this function, only the probability of the expected class is used to evaluate the loss function while the others are merely used for normalization. Furthermore, from the monotonically decreasing loss function with the increasing of p_t and in the limit case of $p_t = 1$ with $L = 0$ we have a function that penalizes small likelihoods for the expected label while simultaneously overlooking the likelihoods associated with wrong classes.

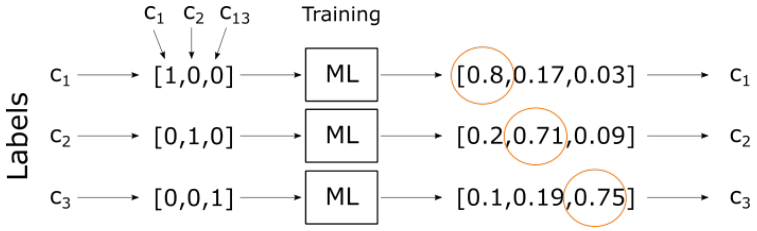

FIGURE 4.3: One-hot encoding of the class labels used in the supervised training where a ML algorithm learns to associate to each index an identification likelihood for the particle.

The last concept we want to introduce corresponds to the process of the interpretation of the results, as well as the metric for its evaluation. In this work, we use the accuracy condensed in confusion matrices to represent the results of each test performed. In short, a confusion matrix has the expected label on one axis and the one predicted by the algorithm on the other, see figure 4.4. The optimal case is when the confusion matrix has the principal diagonal filled since any other filled square signifies confusion from the algorithm. Lastly, to assess the overall accuracy of the model we divide the number of correct predictions by the total number of examples.

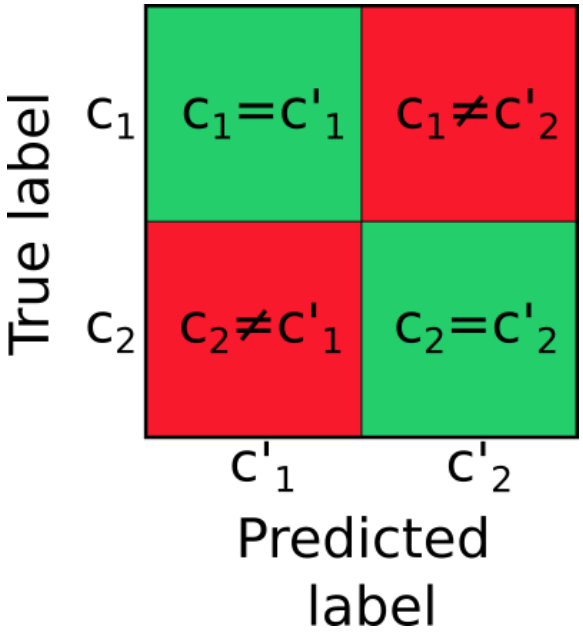

FIGURE 4.4: Confusion matrix scheme for the presentation of classification results where in the diagonal we find the correctly predicted labels, all other being wrong predictions.

4.2 Deploying a CNN classifier for optically trapped particles

As said before, in the last few years deep neural networks have grown in popularity in great part due to the use of GPUs as computing hardware. Nevertheless, being hardware specialized for imaging processing, GPUs architecture is more suitable for algorithms that exploit the use of images as input information, such is the case of the Convolutional Neural Network. In short, a CNN is a Deep Learning method that can take in an input image, assign importance to various characteristics and objects in the image, and classify them. In a CNN, the equivalent to the feature extraction process is performed by a set of special convolution filters and pooling operations withdrawing long and short-range patterns. Furthermore, comparatively speaking to other image classification algorithms, CNNs employ a minimal amount of pre-processing, as the filters or kernels are optimized through automatic learning.

To implement a CNN-based algorithm for the classification of particles we must convert the time series data into image information. There are two main forms of encoding a time series information in an image: encode it in a two dimensional matrix with the dimensions given by the number of signal components times the acquisition time, or encoding in histograms where the image size is fixed by a given number of bins. The former results in images growing with the integration time and longer execution times meaning

slower classifications. The latter has the size controlled by the number of bins while maintaining the statistical information at the cost of the time correlation information. In this work, to minimize the execution time, we will be implementing histogram-based information.

The image creation process consisted of the plotting of 2-dimensional histograms of the transverse position or displacement time series with 2500 time steps of $10^{-4}s$ resulting in $250ms$ segments. In order to avoid automatic bin range detection based on time series extreme points, we standardized the range of bins to a fixed length value. The position histograms are taken from an interval between $[-0.07, 0.07]\ V$ while displacement, typically showing smaller values, was limited between $[-0.02, 0.02]\ V$, see figure 4.5. Furthermore, we used a magnification of the images as a data augmentation technique adding a window for position and displacement of $[-0.02, 0.02]\ V$ and $[-0.005, 0.005]\ V$, respectively. In the last step of data prepping, we normalized the images to the maximum pixel value. The normalization avoids biasing set in the case of an image having a pixel value that exceeds any other in the database.

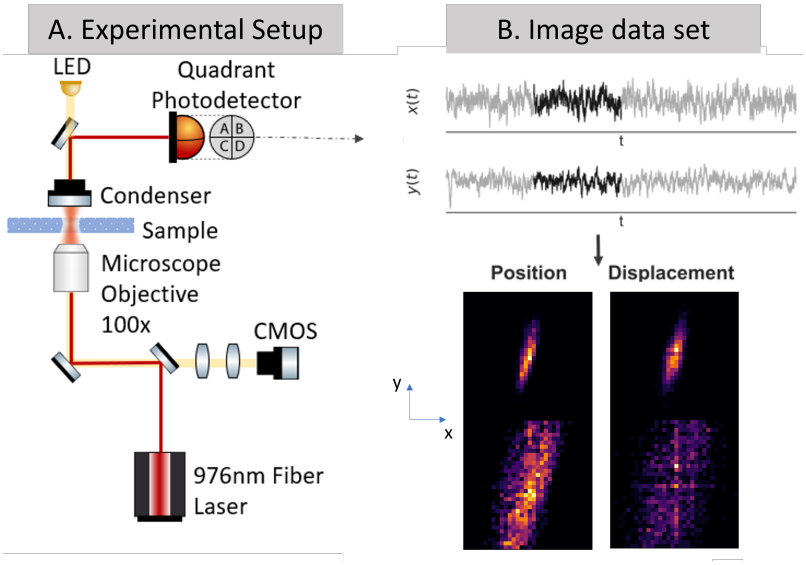

FIGURE 4.5: Image creation scheme from OT trapping and time series acquisition (A) to segmentation and histogram plotting (B).

From the previous chapter, we expect the density distributions to discern based on the variance of the time series. Furthermore, while the variance is typically well established for a given particle the distribution slightly changes with the presence of noise in the frequency counting due to the particle dynamics. Since no two images will ever be exactly the same the ML cannot simply memorize the input thus raising the generalization

capabilities of the model.

4.3 Classification Results

To study the capabilities of CNN for optically trapped particle classification tasks, we will use a fixed architecture as presented in figure 4.6 to perform a series of classification tests consisting of classes of particles with various types and sizes. We have focused on two distinct case studies, described in table 4.1: a first that consisted in classifying particles of distinct materials and a second that consisted in identifying particles of distinct sizes.

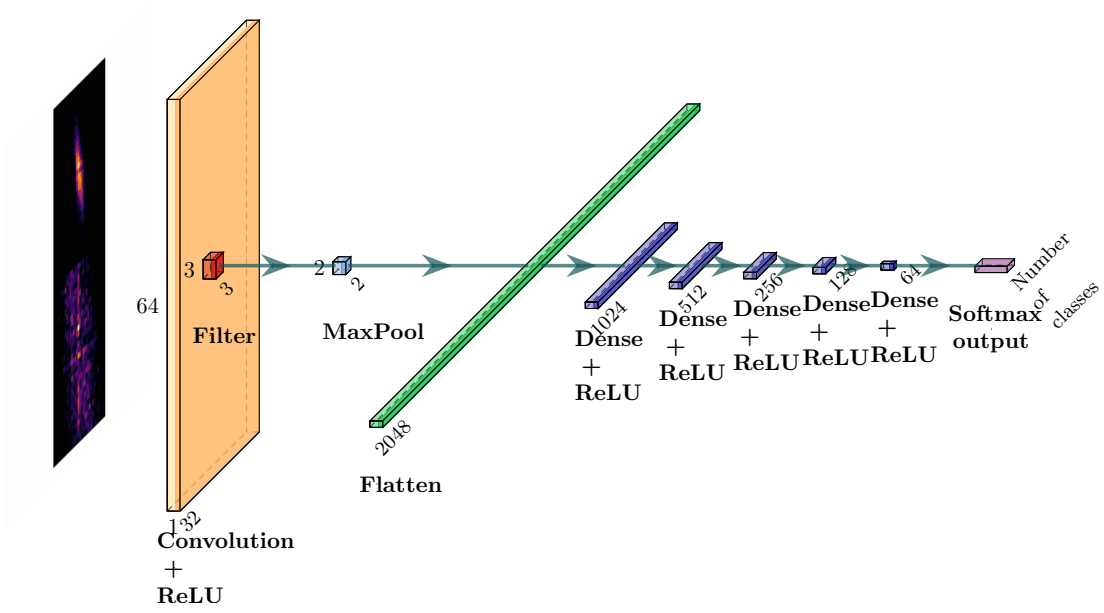

FIGURE 4.6: Implemented CNN architecture featuring, in order, a convolution layer, max-pooling, feature flattening, a five-layered multilayer perceptron and finally a softmax to output a vector of class likelihoods.

The CNN model was deployed in Python 3.7.9 using Keras version 2.3.1 with TensorFlow backend and running on a NVIDIA TITAN V. To compare the two types of information we will be using position and displacement in separate tests. For the evaluation of the model, we utilize k-fold cross-validation commonly used to estimate real-life performance while simultaneously featuring a low bias in data splitting. In short, this method segments the dataset into k folds and uses all but one dataset to train the weights while the remainder evaluates the model, see figure 4.7. By testing the model in unforeseen test samples and iterating both several times, the results highlight the capabilities of the model generalization capabilities.

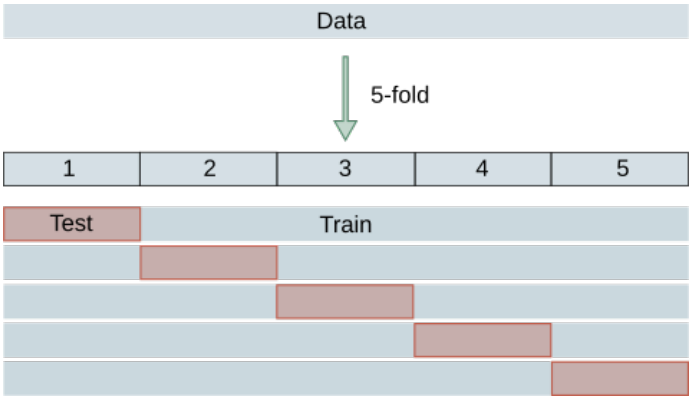

FIGURE 4.7: Data iteration of a 5-fold cross-validation for ML model evaluation. By iteration through distinct training and testing sets, this methods is used to predict the effectiveness of a model generalization capabilities in real life.

	Number of Particles	Type	Size
Case Study 1	10	Polysterene (PS)	$3\mu m$
		Polymethyl methacrylate (PMMA)	
	10	PS	$8\mu m$
		PMMA	
Case Study 2	10	PS	$3\mu m$
			$4\mu m$
			$8\mu m$
	10	PMMA	$3\mu m$
			$8\mu m$

TABLE 4.1: Case studies used to test the CNN for classification of particles differing in either size or type.

4.3.1 Experimental results

The experimental data for each particle in each case study corresponded to a total of $25s$ time series with time steps of $10^{-4}s$, acquired by the quadrant photodetector at an acquisition rate of 10kHz. These segments were then divided into smaller segments of 250 milliseconds, that were used to generate the images as described before.

Starting with case study 1, the results obtained for the type classification task are summarized in figure 4.8. First, we can note that the results largely surpass the pure guess performance even for a large dataset of segments (over 2000), which validates the use of a CNN methodology for this classification task. Also, both position and displacement histograms achieve satisfying results. Position-based achieve 80% accuracy for the $3\mu m$ and 64% for the $8\mu m$, improving to even better results with 88% and 81% when using displacement information.

An overall improvement is observed when using displacement-based histograms rather

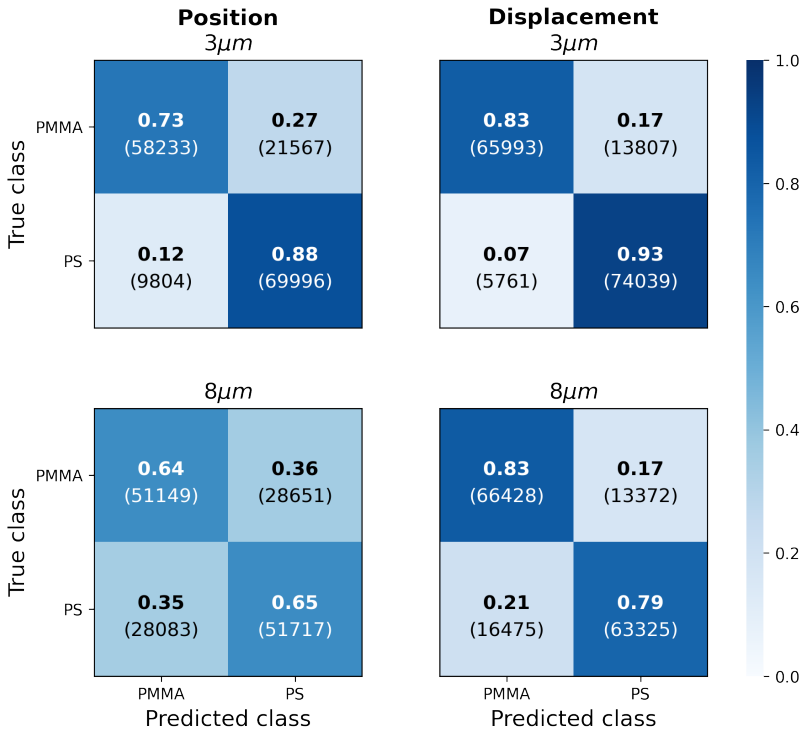

FIGURE 4.8: Type classification results between experimental time series of PS and PMMA particles show good results for the $3\mu m$ sized particles (top row) with 80% and 88% accuracies for position and displacement information, respectively. On the bottom row, position time series are not very efficient with 64% while showing good results for displacement with 81% accuracy.

than position. As previously studied, the position and displacement follow a zero mean gaussian distribution with the variances given by equations 3.4 and 3.7. The distinct encoding of the physical properties of the particles by these equations results in a different level of separability in the variances of the time series. As expected, the displacement histograms are better classified than the position ones, which can be associated with the lower susceptibility to experimental drifts and bias of this signal compared to the position, as discussed in the previous chapter. Indeed, to provide evidence to support this fact, we can analyze the distribution of the variances (thus associated with the transversal size of the histograms) for the distinct types, here represented in figure 4.9. As seen, in addition to smaller variances for each particle, the displacement features a higher degree of separability of the regions for each type.

As for the size classification, i.e. case study 2, summarized in figure 4.10 particles of PMMA can be correctly classified with accuracies around 88% for the position histograms,

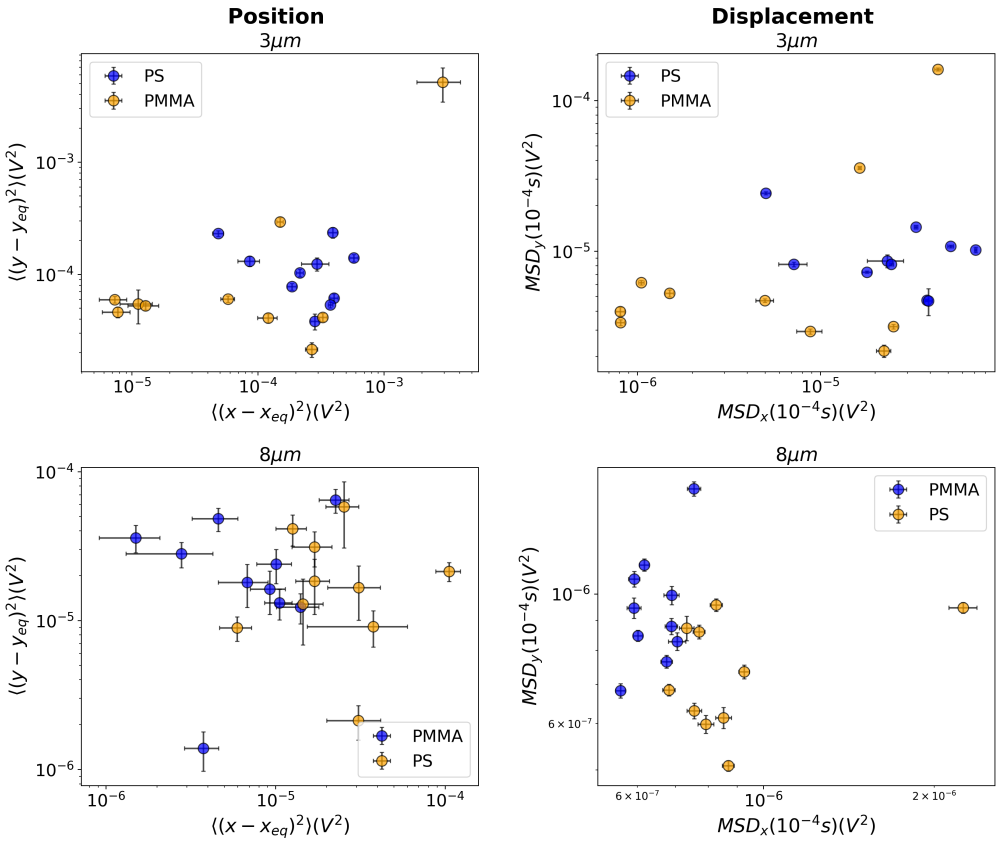

FIGURE 4.9: Position (left) and displacement (right) time series variances in the transverse plane for $3\mu m$ (top row) and $8\mu m$ (bottom row) sized particles where a clustering effect is showed when transitioning from implementing position information to displacement (left to right).

and 99% for displacement-based histograms. In its turn, PS particles feature overall accuracies of 74% and 71%, with the lower performance being associated with the confusion of the intermediate size $4\mu m$, as interpreted from the confusion matrix.

4.3.2 Synthetic results

In order to validate the experiments and assist in the interpretation of the results, we numerically simulated our experimental procedure, using the digital twin developed in the previous chapter. The simulations are performed with the physical quantities (τ_{ot}, D) extracted directly from the experimental time series via the PSD method. The time series generated consists of 2.5×10^7 points with time steps of $10^{-6}s$, by striding 100 steps we get a $25s$ position time series with time steps of $10^{-4}s$, which corresponds to the same configuration as the experimental data.

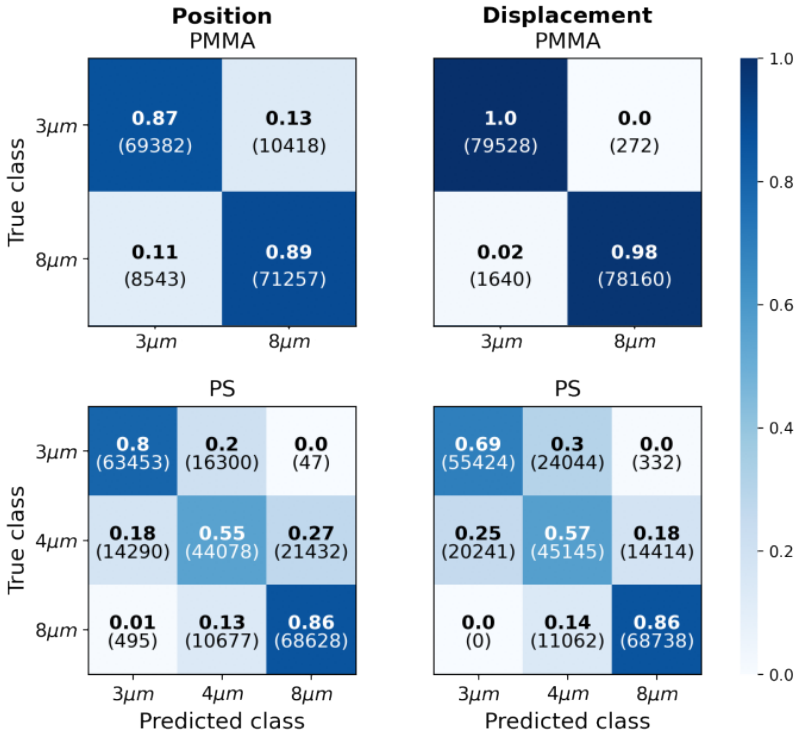

FIGURE 4.10: Size classification of experimental time series shows very good and even excellent results for PMMA bead (top row) classification between $3\mu m$ and $8\mu m$ particles with 88% for position and 99% accuracy using displacement time series. In comparison, for PS particles, only satisfying results are obtained with 74% and 71% for position and displacement, respectively.

As before, we first focus on the first case study 1, i.e. the classification between particles of distinct composition. The results presented in figure 4.11 show that using position-based histograms the classification results obtained only a modest accuracy of 74% and 59% for $3\mu m$ and $8\mu m$ particles respectively. Nonetheless, as happens with the experimental results, we observe improvements when using displacement information instead of position with average accuracy improvements of 18% and 9% for the $3\mu m$ and $8\mu m$ sized particles, respectively, which aligns with the observations obtained with the experimental data.

For Case Study 2, we obtained the results that are summarized in figure 4.12. Firstly, PMMA particles with a considerable size difference are easily distinguished at average accuracies of 87% and 99%, thus showing again an improvement of 12% when using displacement-based histograms. The second experiment for PS particles features an additional $4\mu m$ size, sitting in between the $3\mu m$ and $8\mu m$. The results feature lower accuracy of 72% for position information, but again with an improvement of 6% to 78% while using

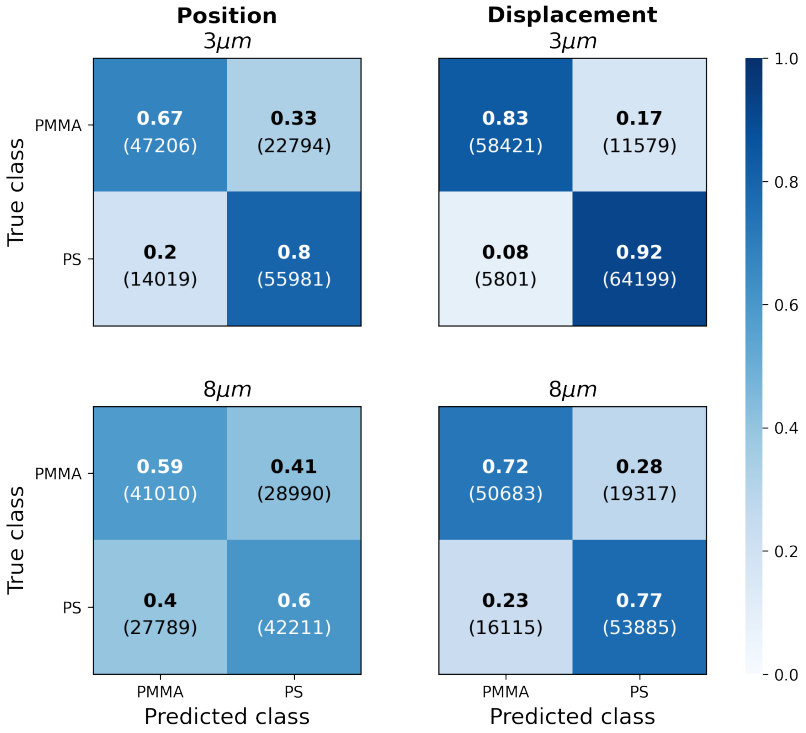

FIGURE 4.11: Type classification between simulated PS and PMMA particles showing satisfactory and good results for $3\mu m$ sized particles (top row) with 74% and 88% accuracy for position and displacement information, respectively. Meanwhile, for $8\mu m$ beads (bottom row) the results are not as efficient nevertheless showing satisfactory results with 59% and 75% accuracy for position and displacement, respectively.

displacement. Again the results obtained using the digital twin largely align with those of the experimental results, validating our methodology.

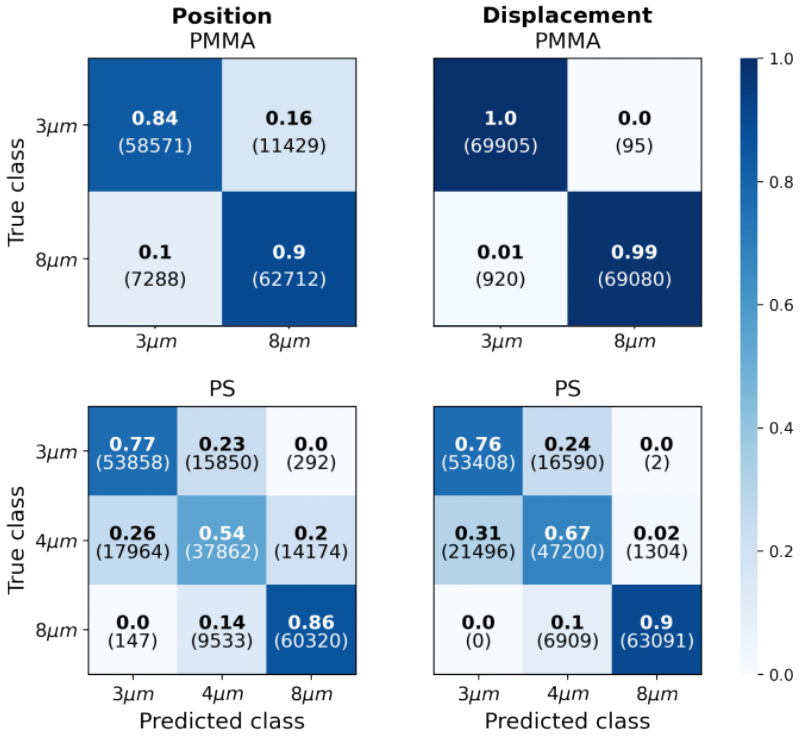

FIGURE 4.12: Size classification of simulated particles where very good and excellent results are obtained for PMMA (top row) with 87% and 99% accuracy for position and displacement, respectively. In comparison, only satisfying to good results are obtained for PS beads (bottom row) with 72% and 78% accuracy using position and displacement.

4.4 Concluding remarks

In this chapter, we described our efforts to deploy a CNN-based classifier for optically trapped particles based on the forward scattered signal. For that, we first reviewed some introductory concepts of NN, before discussing the process of transforming the acquired time series into an image in the form of a histogram, thus acting as the input information to the CNN model.

We then focused our attention on two distinct case studies, evaluating a CNN with fixed architecture on the classification task of optically trapped particles based on either size or composition. For both cases, it features satisfying results using position-based information that is improved using displacement-based histograms, which we found to be associated with a higher separability of the mean squared displacement comparatively with the position variance.

On one hand, these results highlight not only the capability of CNNs for the classification of optically trapped particles but also the possibility for the application of displacement as a novel source of information to be used in classification routines. For example, using speckle patterned "sieves"[37] together with CNN of the position and displacement information has the potential to achieve higher classification results without the requirement for longer integration times.

On the other hand, compared to previous works, the implemented methodology works with smaller time intervals (250 milliseconds versus 500 milliseconds of reference [15] and 2 seconds in [56]), thus allowing to perform faster classifications. Furthermore, being based on highly optimized libraries for CNNs, the computation of the prediction is almost real-time (a few milliseconds), which means that it can deliver faster classification rates as it bypasses the use of time-consuming processes for feature extraction.

Finally, we also draw attention to the usage of the digital twin, which to our best knowledge was never exploited in the literature for these purposes. This innovative approach may allow us to understand how the time interval between positions, bin number, and time length of each time series affects the results, thus playing an important role in the study of optimizations and limitations of this technique.

Chapter 5

Towards real-time particle classification with Reservoir Computing

In the previous chapter, we saw how a CNN-based classifier could be a valuable tool for trapped specimen classification. Yet, despite its success, it still requires acquisition times of around 250 milliseconds, which can be unsuitable for tasks requiring a very high throughput.

In this context, we will explore in this chapter the concept of Reservoir Computing, seeking to use it as a suitable Neural Network tool for real-time and online classification of optically trapped particles. As a model, we consider an *in silico* Echo State Network, considering the possibility of transitioning to an optical computing implementation of the same architecture.

With this objective, we start by describing the fundamentals of ESN accordingly to Herbert Jaeger[81] and the algorithm used for classification. Lastly, we test the ESN architecture for the classification of particles with both synthetic and experimental data.

5.1 Fundamentals of echo state networks

This section presents the fundamental principles to construct an ESN for a discrete-time reservoir as presented in [81]. We start by defining at a time step n the input vector of features $\mathbf{u}(n) = \left(u_1(n), u_2(n), ..., u_K(n)\right)$, reservoir state $\mathbf{x}(n) = \left(x_1(n), x_2(n), ..., x_N(n)\right)$ and outputs $\mathbf{y}(n) = \left(y_1(n), y_2(n), ..., y_L(n)\right)$. Illustrated in figure 5.1, the connections

between the three layers are made through real-valued weight matrices $\mathbf{W}_{in}$ of $N \times K$ connecting the input features to the nodes in the reservoir, $\mathbf{W}$ of $N \times N$ representing the reservoir inner interactions, $\mathbf{W}_{out}$ of $L \times (K \times L \times N)$ of the input, reservoir and previous output state contributions and lastly $\mathbf{W}_{back}$ of $N \times L$ of the output feedback to the reservoir.

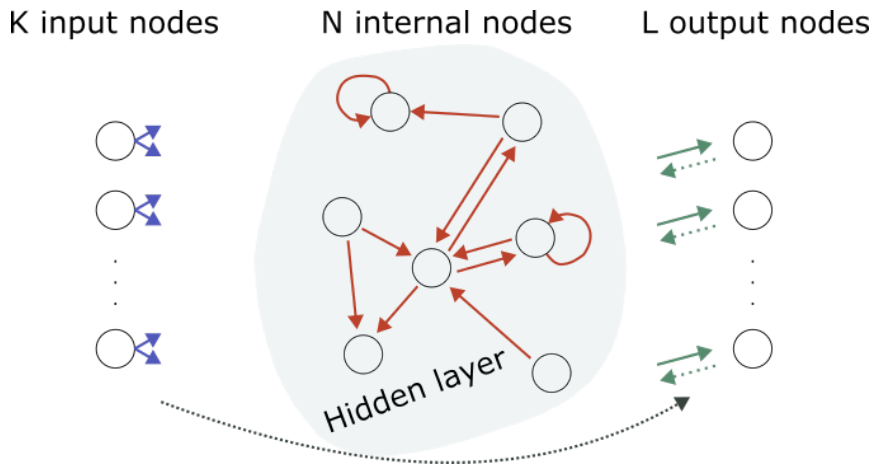

FIGURE 5.1: Visualization of the ESN architecture featuring the possible node connections and layer dimensions.

The reservoir dynamics evolve according to the linear mapping of input information onto an N-dimensional space followed by a nonlinear transformation given by

$$\mathbf{x}(n+1) = f\left(\mathbf{W}_{in} \cdot \mathbf{u}(n+1) + \mathbf{W} \cdot \mathbf{x}(n) + \mathbf{W}_{back} \cdot \mathbf{y}(n)(n) + C\eta\right), \tag{5.1}$$

where f is the element-wise activation function and $\eta \in [0,1]$ is a noise factor generated from a uniform distribution scaled by the constant factor C. Typically, for in silico computing, we take the *tanh* activation function. Furthermore, throughout this work we do not consider the feedback of the output into the system ($\mathbf{W}_{back} = \mathbf{0}$).

The advantage of using a non-adaptative reservoir with non-linear dynamics as the hidden layer is its capability for randomly projecting a non-linear input to a high N-dimensional space from where the separation of features becomes a linear problem of adjusting the readout. In turn, the requirement for weight optimization of the hidden node layers is lifted thus resulting in faster and more efficient training performed in the output layer alone, although more complex methods are also applicable[61]. Since we do not need to train the reservoir, this methodology is suitable for physical implementation with passive reservoirs resulting in low energy consuming and fast physical computation devices[62].

In some cases, the problem at hand may require reservoirs with longer-term memory. A way of solving this is by introducing leakage of the previous to the posterior state of the reservoir by means of an equation

$$\mathbf{x}'(n+1) = (1-\alpha)\,\mathbf{x}(n) + \mathbf{x}(n+1)\,, \tag{5.2}$$

where $\alpha \in [0,1]$ is the leaking rate[81, 82].

By means of recurrence and leakage, a reservoir possesses long and short-term memory of the input. Still, for solving realtime machine learning problems and for convergence of the ESN it is important that the memory of the input decays. For ESN this is called the Echo State Property (ESP) which guarantees that the state at a given time is dependent until a finite time in the past inputs. The conditions for ESP vary depending on the reservoir matrices but for the purposes of this work a sufficient condition is $\sigma(\mathbf{W}) < 1$ where $\sigma(\mathbf{W})$ is the maximum eigenvalue of $\mathbf{W}$[83, 84].

5.2 RC Algorithm: an in silico Echo-state network

The RC algorithm written for the classification of particles follows the simplest model of ESN presented in the previous chapter to account for the feasibility of a future all-optical integration for intelligent OT setups. Nevertheless, we should stress that the model we implement in silico still does not have a direct translation to physical implementation as the input has prior processing not able to be performed optically e.g. transversal position determination by the quadrants in the photodiode.

In figure 5.2 we represent the scheme of the ESN built. The random weights of input-reservoir and reservoir-reservoir mapping are generated using scipy sparse allowing to control matrix density and NumPy randn with unit variance permitting scaling which together adjust for non-linearity and memory control. The input matrix is scaled by a constant factor while the reservoir matrix is scaled to have a maximum eigenvalue to respect the ESP condition.

The information is fed at the input layer to the network starting with an initial state as the zero state vector. The state's history is then computed by iteration of equations 5.1 and 5.2. For the activation function, we can use the *tanh* whose optical implementation can be achieved with saturable absorbers or amplifiers although counting with energetic caveats[63, 65]. In the scope of the prospective work discussed in the final chapter, a *sine*

will be implemented as the activation function for the nodes. This sinusoidal activation function has been previously demonstrated to be possible in a one-node reservoir with virtual nodes created by a delay line analogous to the traditional architecture[64].

Using the ESP, we remove the initialization bias of the reservoir by dropping a transient time until the initial state of the system is forgotten. We then start recording the states of the system after the transient time passes. The final step consists in using the history of states computed from the training sample to determine the output weights yielding the final result. Three methods of using the history of states are easily applicable: full history, time-averaged state, and last state[61]. The last step of finding the readout weights is performed via the Ridge regression from the python package *sklearn* that minimizes the linear least squares function subjected to a regularization to avoid overfitting. Other readout methods are possible to be applied computationally such as support vector machines, elastic net penalty and multilayer perceptron[85, 86], but are left out of the scope of this dissertation.

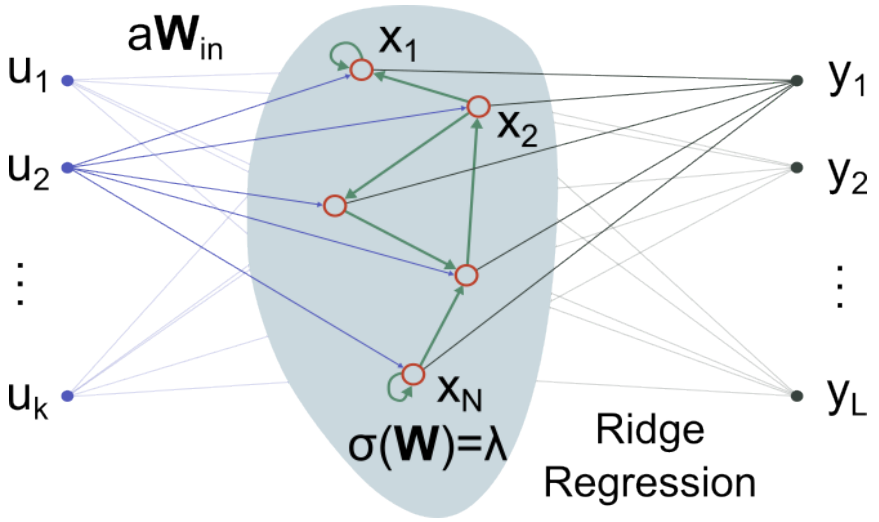

FIGURE 5.2: Design of the implemented ESN model featuring the input and reservoir scaling factors together with the ridge regression method used to train the output layer weights.

The hyperparameters of the model used are presented in table 5.1 together with a description and role in the network dynamics with insights as given in reference [81, 87]. Lastly, we note that optimization algorithms should be applied to search the space of hyperparameters for achieving the best results for a validation data set. Two widely used methods are the grid search and stochastic gradient descent[82]. Unfortunately, due to long time requirements for proper use of either method, these were not possible to be implemented.

Hyperparameters	Description
Number of nodes: 300	Defines the size of the high-dimensional space the input is mapped into.
Input scale: 10	Alters the magnitude of the input consequently making it fall into different regions of the activation function. Therefore this controls the level of non-linearity.
Spectral radius: 0.99	Maximum eigenvalue of **W**. This value controls the memory longevity of the reservoir and whether the ESP condition is verified. Bigger(smaller) values result in longer(shorter) term memory.
Leak rate: 0.8	State update speed defining how fast a state drifts from previous states.
W density: 0.1	Controls the number of connections in the reservoir. Advised to be sparse, thus allowing subnetworks in the reservoir with isolated dynamics.
$\mathbf{W}_{in}$ density: 1	Number of connections of the input into the nodes of the reservoir. A dense matrix is recommended.
Transient time: 10	Time steps until the algorithm starts to record states of the reservoir. This time is used to remove the bias of the initial state of the reservoir.
Noise: 2	Noise scalling factor. It improves generalization capability of the ESN by wobbling the states around the stable path defined by the input.

TABLE 5.1: Presentation of the hyperparameters used in the ESN model (left) together with the effect the parameters bring upon the data processing (right) as described in the references [81, 87].

5.3 Results

In this section we implemented the ESN algorithm developed in the two case studies of the last chapter, using both position and displacement time series as input information. We are interested in testing the ESN framework and comparing the two information sources. As in the previous chapter, we will resort to both synthetic and experimental data for classification purposes.

5.3.1 Experimental data classification

The experimental data for each particle was recycled from the previous section with a different segmentation to speed up the evaluation process. From the total 25s time series

with time steps of $10^{-4}s$, acquired by the quadrant photodetector at an acquisition rate of $10kHz$, only $5s$ are used and are segmented into $100ms$ time series.

For case study 1, which seeks classification based on particle type, the results are presented in figure 5.3. To start our analysis, we notice how the results using position time series are only slightly above the pure guess with 63% and 54% accuracies, while for displacement the guess is more inclined towards the correct answer. Although some improvement can be seen for the displacement time series, the performance only reaches satisfying levels of 68% and 66% accuracies for the smaller and bigger-sized particles, respectively.

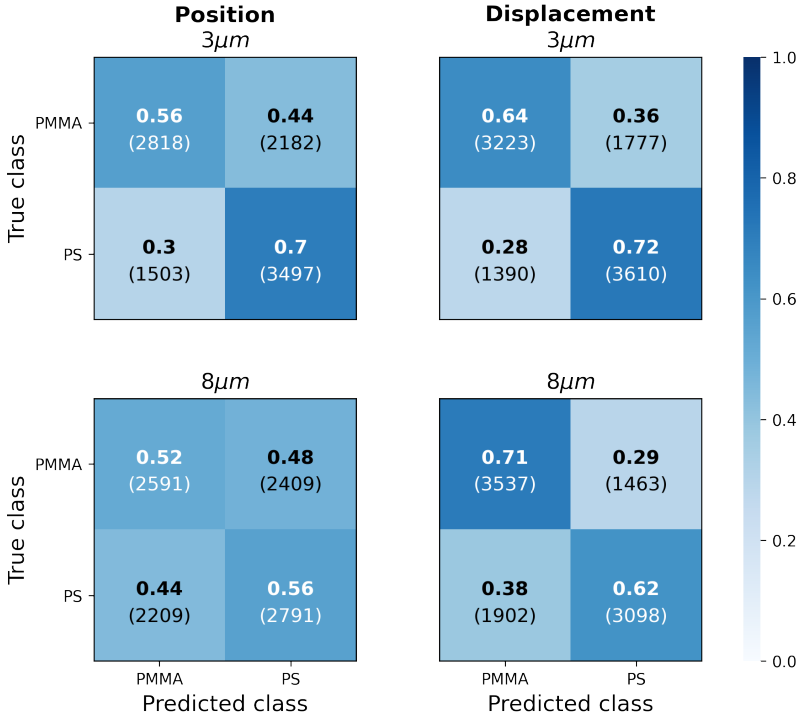

FIGURE 5.3: Classification using RC between experimental PS and PMMA particles which show for $3\mu m$ beads (top row) only slightly above pure guess with 63% and 54% accuracies for position and displacement time series, respectively. And with similar results for the $8\mu m$ particles (bottom row) with 68% and 66% for position and displacement.

As for the second case study concerning the classification of particles in size, the results are condensed in figure 5.4. We can see that the RC algorithm performs rather well for classifying PMMA particles with 77% using position time series and improving to 93% with displacement series. As for the second set of tests classifying PS particles differing in size, a low confusion between the smaller and bigger-sized particles is still observed.

Nevertheless, a higher confusion arising from the presence of an intermediate-sized particle achieves only 59% and 70% accuracy using position and displacement time series.

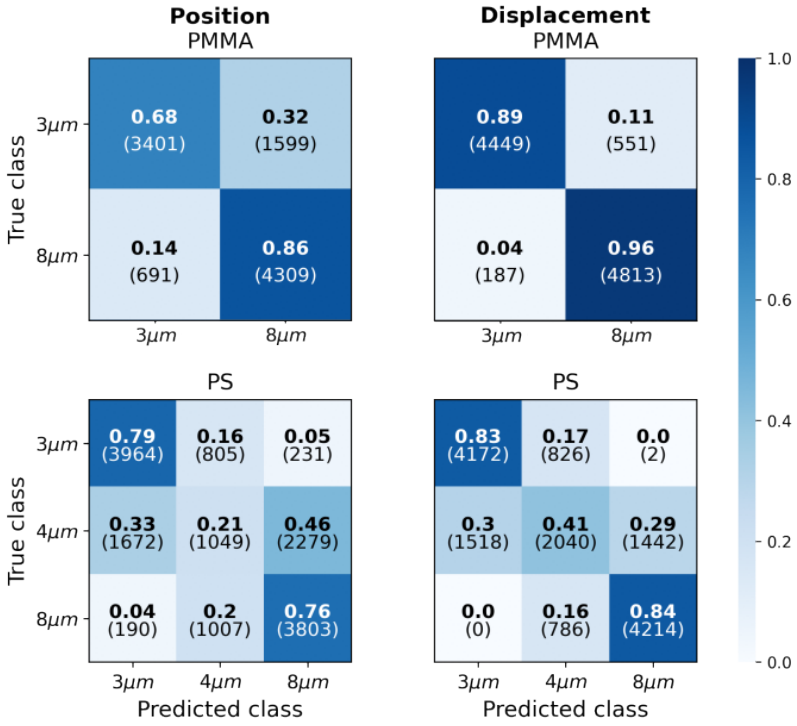

FIGURE 5.4: Size classification of experimental data shows good results for the PMMA particle (top row) classification with 77% and 93% accuracy while a higher confusion due to an intermediate-sized particle allows only to obtain 59% and 70% accuracy for position and displacement time series, respectively

5.3.2 Synthetic data classification

The validation of the experimental results was again performed through numerical simulations. The simulated time series is the previously generated data set but we limited them to a total of 5s with time steps of $10^{-4}s$, divided into 100ms segments. Furthermore, since we will be dealing with the direct time series, a random white noise corresponding to 0.1% of the maximum values is added at the input of the ESN for simulating true experimental conditions.

Starting once more with classification between particle compositions, see figure 5.5, the results relate to those observed for experimental values of 63% and 64% accuracy for the smaller particles with position and displacement information, respectively, while for the bigger sized particles 54% accuracy is observed for both sources of information.

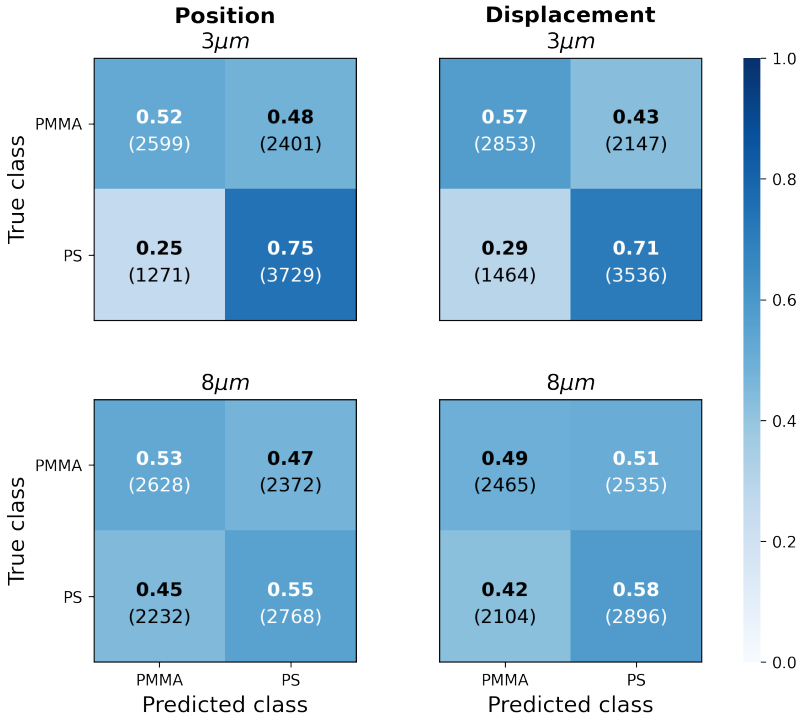

FIGURE 5.5: Classification using RC to identify between PS and PMMA particles showing only above pure guessing for all tests performed with 63% and 64% accuracies for $3\mu m$ sized particles using position and displacement and 54% accuracy for $8\mu m$ beads for both sources of information.

Finally, and to conclude our series of tests presented in figure 5.6, size classification closely follow the results obtained experimentally. For PMMA particle classification between smaller and bigger digital particles resulted in 65% and 100% using position and displacement time series, respectively. For the PS particles, the classification using position time series resulted in 51% while using displacement improves the classification to 74%. In both cases short to no confusion between $3\mu m$ and $8\mu m$ sized particles occurs while the presence of an intermediary $4\mu m$ sized class of particles raises confusion.

Consistently with the previous results, the displacement obtains superior classification results when compared with the position.

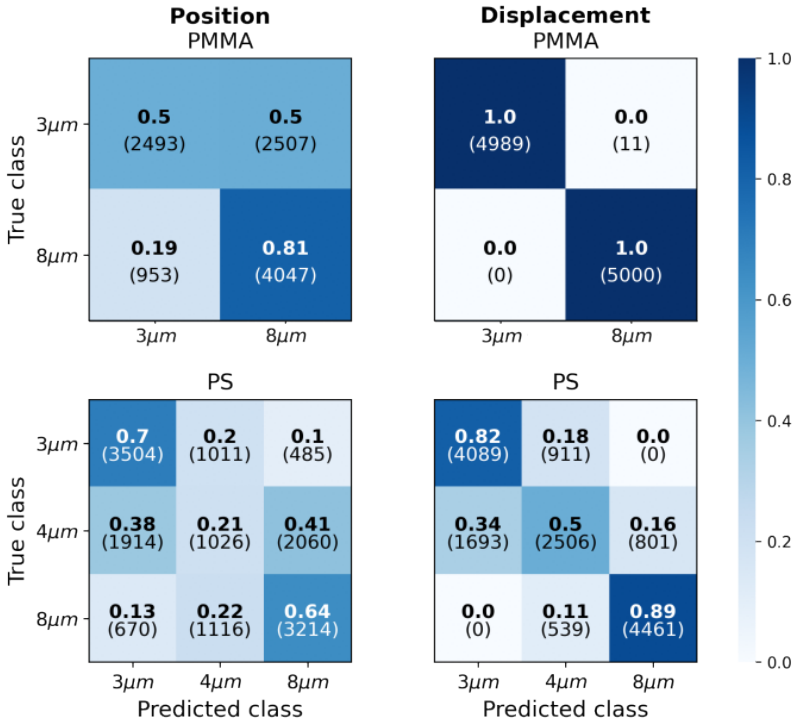

FIGURE 5.6: Size classification results follow those observed experimentally with 65% and 100% accuracies using position and displacement for PMMA particles (top row) and 51% and 74% accuracies for PS particles where the confusion is raised due to the presence of an intermediate $4\mu m$ particle.

5.4 Concluding remarks and discussion

In this chapter, we explored the implementation of an RC for the task of real-time classification of optically trapped particles. For that goal, we reviewed the fundamental concepts of RC with a focus on ESN, prior to its digital implementation using *Python* programming language.

We then tested the ESN framework with fixed architecture on two distinct case studies of classification between the composition or size of the particles. For the case of size classification, we can obtain good results for the identification of $3\mu m$ and $8\mu m$ particles. Nevertheless, when introducing intermediate-sized particles we observe a decay in the accuracy pointing towards either a lack of resolution from the algorithm or the presence of outlier particles that cross over class limits. In agreement with the results from the previous chapter, the displacement comes again in aid of improved classifications. Unfortunately, for the type classification, the results using position time series barely leave what

would be obtained by randomly guessing while displacement obtains slightly improved results but still falls short of results obtained using CNN.

While the results obtained are not indicative of effective classification for both case studies, we emphasize that this work explores only an infinitesimal part of the space of configurations of ESNs and of the time series parameters, such as sampling rate and integration times which affect the time series correlation and simultaneously the variance of the displacement. Also, by directly using the time series as input for classification, we are more susceptible to noise coming from the measurements which for example in histograms are accommodated by the binning step. Furthermore, growing the data set either by means of new measurements or data augmentation techniques can lead to improved results.

Nevertheless, in spite of all the limitations, we still stress that we were successful in applying an RC-based classifier for the specific case of particle size classification. This finding proves the concept of real-time classification based on the forward scattering signal and thus sets the stage for future work that can explore the parameter space in more detail.

Chapter 6

Conclusions and outlook

This major goal of dissertation was the exploration of faster and more accurate classification of optically trapped particles by exploring the Brownian dynamics encoded in the forward scattered signal. In particular, we search to take advantage of the intrinsic feature extraction of CNN and their GPU accelerated execution times to achieve this goal. Furthermore, by implementing RC we have a first glance at the possibility of real-time classification of particles.

For this purpose, we started by studying the physical principles behind optical micromanipulation for effective 3D trapping of transparent particles, gaining an intuition of the phenomena that is OT. From a balance between optically induced gradient and scattering forces, OT uses a tightly focused beam like those obtained by the inverted microscope configuration explored in the experimental part of this dissertation together with a quadrant photodetector to acquire trapped particle position time series. Implementing this setup in the laboratory, we designed an experimental procedure and acquired a data set of particle positions in reproducible manners, to avoid unwanted bias as required by machine learning applications.

From experimental procedure to modelling of the dynamics and construction of a digital twin, we review the Langevin model describing the behaviour of a trapped particle accounting for the Brownian dynamics, optical trapping by a gaussian beam and viscous damping. As an alternative representation of the particle position time series which can feature unwanted drift effects, we propose the usage of displacement as a novel source of information which filters the long-term drift effects.

Then, by integrating the overdamped Langevin equation using the well-known RK4

we build a digital twin to the experimental setup implemented. By a series of tests performed on this simulator, we verify its convergence towards the initial statistical values.

Finally, we implement the CNN to position or displacement time series histograms. We start by discussing the process of image creation which requires standardization of bin ranges and normalization of images to unity. Classification tests are performed on experimental data having their results supported by the usage of simulations. Implementing a fixed CNN architecture, we tested the performance of the model on two case studies of either classification between size or composition which confirmed the possibility of implementing this technique for the classification of particles using $250ms$ time series (faster than previously implemented methods[15, 56]). From our results, we emphasize the usage of displacement time series which achieved higher accuracies in the majority of the tests performed.

To conclude our journey, we have a first glance at the implementation of RC for the possibility of real-time analysis in OT setups. Starting with a review of the fundamentals of ESN, then used in the digital implementation in python. Classification test results between types are short of leaving what would be obtained by random guessing the particle classes. In contrast, the classification of particles based on the sizes between $3\mu m$ and $8\mu m$ shows classification capabilities.

6.0.1 Prospective work

The results enclosed in this dissertation may span its impact across some unexplored doorways that may be explored in future research in the short to medium term.

On one hand, the successful classification of particles using CNN call for an exploration of distinct trap profiles. These can be shaped by HOT, and may introduce other symmetries, lattices, or even more exotic force fields such as speckle patterns demonstrated to be capable of sorting particles[37]. Joining these methods with both position and displacement time series can result in considerable improvements to the task without the cost of time. Furthermore, we highlight the usage of the digital twin developed in this work for the improvement and study of the limits of these techniques for the classification of trapped particles by optimization of a series of parameters e.g. bin number, acquisition times, and even CNN architectures.

On the other hand, with the proof-of-concept of the RC algorithm for the classification of particles, and leaning toward the physical implementation of this framework, real-time classification of optically trapped particles may be implemented in microelectronic systems and even on all-optical systems taking advantage of the light speed. Indeed, the group at INESC TEC has recently devised an optical RC framework sitting on amplitude or phase encoding and the non-linearity from the light measuring to be implemented as a near-all-optical classifier and some efforts have been made towards the use of this system for OT setups. Yet, in spite of our best attempts to implement such a system, significant effort and research are still needed to realize such an advanced concept. Lastly, we must call attention to the exploration of the digital twin to optimize and search for limitations of the model which might lead to interesting breakthroughs.

Appendix A

Trapped Brownian motion physical means

The determination of the moments of the distribution for the position and displacement time series is pivotal to understanding the differences between the usage of either type of information. We dedicate this appendix to the calculations leading to the MSD equation valid in the overdamped regime of trapped Brownian motion. Furthermore, as we move towards faster time classification the validity of the overdamped approximation of the Langevin equation fades and we require to use of the full model description. Therefore, for future reference, we leave the calculations of the MSD for the full Langevin model.

A.1 Mean squared displacement

Overdamping approximation:

We begin with the solution to the non-homogeneous linear differential overdamped Langevin equation 3.2,[39] obtained by applying the integrating factor method

$$\mathbf{r}(t) = \mathbf{r}(0)\, e^{-\frac{t}{\tau_{ot}}} + \sqrt{2D} \int_0^t e^{-\frac{(t-s)}{\tau_{ot}}} \chi(s)\, ds, \tag{A.1}$$

where $\mathbf{r}(0)$ is the initial position.

Plugging this solution into the MSD, equation 3.5, definition we get

$$\begin{aligned}\mathbf{MSD}\left(\Delta t\right) &= \left\langle \left[\mathbf{r}\left(t+\Delta t\right)-\mathbf{r}\left(t\right)\right]^2\right\rangle \\ &= \left\langle \left[\mathbf{r}\left(0\right)e^{-\frac{t}{\tau_{ot}}}\left(e^{-\frac{\Delta t}{\tau_{ot}}}-1\right)+\sqrt{2D}e^{-\frac{\Delta t}{\tau_{ot}}}\int_0^{t+\Delta t}e^{-\frac{(t-s)}{\tau_{ot}}}\boldsymbol{\chi}\left(s\right)ds-\sqrt{2D}\int_0^t e^{-\frac{(t-s)}{\tau_{ot}}}\boldsymbol{\chi}\left(s\right)ds\right]^2\right\rangle\end{aligned} \tag{A.2}$$

where $\langle(...)\rangle$ is the mean over an ensemble of random walks followed by an average over time. Using the properties of Brownian motion $\langle\boldsymbol{\chi}\left(t\right)\rangle = 0$ and $\langle\boldsymbol{\chi}\left(t\right)-\boldsymbol{\chi}\left(s\right)\rangle = \boldsymbol{\delta}\left(t-s\right)$ over an ensemble of random walks results in

$$\begin{aligned}\mathbf{MSD}_{od}\left(\Delta t\right) &= \langle \mathrm{r}^2\left(0\right)e^{-\frac{2t}{\tau_{ot}}}\left(e^{-\frac{\Delta t}{\tau_{ot}}}-1\right)^2+2De^{-\frac{2\Delta t}{\tau_{ot}}}\int_0^{t+\Delta t}\int_0^{t+\Delta t}dsds'e^{-\frac{2t-s-s'}{\tau_{ot}}}\boldsymbol{\delta}\left(s-s'\right) \\ &+2D\int_0^t\int_0^t dsds'e^{-\frac{2t-s-s'}{\tau_{ot}}}\boldsymbol{\delta}\left(s-s'\right)-4De^{-\frac{\Delta t}{\tau_{ot}}}\int_0^{t+\Delta t}\int_0^t dsds'e^{-\frac{2t-s-s'}{\tau_{ot}}}\boldsymbol{\delta}\left(s-s'\right)\rangle \\ &= \langle \mathbf{r}^2\left(0\right)e^{-\frac{2t}{\tau_{ot}}}\left(e^{-\frac{\Delta t}{\tau_{ot}}}-1\right)^2+2De^{-\frac{2\Delta t}{\tau_{ot}}}\int_0^{t+\Delta t}dse^{-2\frac{t-s}{\tau_{ot}}} \\ &+2D\int_0^t dse^{-2\frac{t-s}{\tau_{ot}}}-4De^{-\frac{\Delta t}{\tau_{ot}}}\int_0^t dse^{-2\frac{t-s}{\tau_{ot}}}\rangle \\ &= \langle \mathrm{r}^2\left(0\right)e^{-\frac{2t}{\tau_{ot}}}\left(e^{-\frac{\Delta t}{\tau_{ot}}}-1\right)^2+D\tau_{ot}\left(1-e^{-2\frac{t+\Delta t}{\tau_{ot}}}\right) \\ &+D\tau_{ot}\left(1-e^{-2\frac{t}{\tau_{ot}}}\right)-2D\tau_{ot}e^{-\frac{\Delta t}{\tau_{ot}}}\left(1-e^{-2\frac{t}{\tau_{ot}}}\right)\rangle\end{aligned} \tag{A.3}$$

Lastly, averaging over a time interval $T >> \tau_{ot}$ results in

$$\mathbf{MSD}_{ot}\left(\Delta t\right) = 2D\boldsymbol{\tau}_{ot}\left(1-e^{-\frac{\Delta t}{\tau_{ot}}}\right). \tag{A.4}$$

A.1.1 Exact solution:

Similarly to the previous case, we begin with the formal solution to the differential Langevin equation 3.1. The procedure to determine the solution of the Langevin equation closely follows reference [73]. As usual we begin with solving the homogeneous equation resulting in

$$r_0\left(t\right) = Ae^{\omega_+ t}+Be^{\omega_- t}, \tag{A.5}$$

with $\omega_\pm = \left(-\gamma/m \pm \sqrt{\left(\gamma/m\right)^2-4k/m}\right)/2$. Applying the variation of constants method the coefficients become dependent on time and the Langevin equation admits the solution

$$r_0\left(t\right) = A\left(t\right)e^{\omega_+ t}+B\left(t\right)e^{\omega_- t}, \tag{A.6}$$

where the coefficients A(t) and B(t) must satisfy the relations

$$\begin{aligned} e^{\omega_+ t}\frac{dA}{dt} + e^{\omega_- t}\frac{dB}{dt} &= 0 \\ \omega_+ e^{\omega_+ t}\frac{dA}{dt} + \omega_- e^{\omega_- t}\frac{dB}{dt} &= 0, \end{aligned} \tag{A.7}$$

where we omit the time dependence of the coefficients to simplify the notation.

Solving the system of equations gives the time derivatives of the coefficients

$$\begin{aligned} \frac{dA}{dt} &= \frac{1}{\omega_- - \omega_+} e^{-\omega_+ t}\frac{\gamma\sqrt{2D}}{m}\chi(t) \\ \frac{dB}{dt} &= \frac{1}{\omega_- - \omega_+} e^{-\omega_- t}\frac{\gamma\sqrt{2D}}{m}\chi(t). \end{aligned} \tag{A.8}$$

Integrating, the coefficients are given by

$$\begin{aligned} A(t) &= \frac{\gamma\sqrt{2D}}{m(\omega_+ - \omega_-)}\int_0^t ds e^{-\omega_+ s}\chi(s) + A(0) \\ B(t) &= -\frac{\gamma\sqrt{2D}}{m(\omega_+ - \omega_-)}\int_0^t ds e^{-\omega_- s}\chi(s) + B(0). \end{aligned} \tag{A.9}$$

Replacing this in equation A.6 results in the solution

$$\begin{aligned} r(t) = &\frac{\gamma\sqrt{2D}}{m(\omega_+ - \omega_-)} e^{\omega_+ t}\int_0^t ds e^{-\omega_+ s}\chi(s) + A(0)e^{\omega_+ t} \\ &- \frac{\gamma\sqrt{2D}}{m(\omega_+ - \omega_-)} e^{\omega_- t}\int_0^t ds e^{-\omega_- s}\chi(s) + B(0)e^{\omega_- t}. \end{aligned} \tag{A.10}$$

The determination of $A(0)$ and $B(0)$ can be obtained using the velocity as a second equation. Taking the mean over an ensemble of random walks and averaging over time removes the dependence of the MSD on the initial conditions of the system. Therefore, we won't be required to determine the expression for the initial conditions we require simply for them to be finite.

Plugging this solution into the MSD definition and computing the mean in a ensemble of random walks and averaging over a time interval analogously, to the overdamping case we get

$$\begin{aligned} MSD_{ex}(\Delta t) &= \langle\langle [r(t+\Delta t) - r(t)]^2 \rangle\rangle \\ &= \frac{4\gamma^2 D}{m^2(\omega_+ - \omega_-)(\omega_+ + \omega_-)}\left[\frac{1}{\omega_+}\left(1 - e^{\omega_+ t}\right) + \frac{1}{\omega_-}\left(1 - e^{\omega_- t}\right)\right] \end{aligned} \tag{A.11}$$

A.2 Autocorrelation

A.2.1 Overdamping approximation:

The position autocorrelation defined as

$$C\left(t+\Delta t,t\right):=\left\langle \mathbf{r}\left(t+\Delta t\right)\mathbf{r}\left(t\right)\right\rangle \tag{A.12}$$

is a measure similarity between the position and consecutive times. Replacing the equation A.1 in A.12 and using the Brownian motion properties and averaging in a time interval T we have

$$\begin{aligned}
C\left(t+\Delta t,t\right) &= \langle\langle\left[r\left(0\right)e^{-\frac{t}{\tau_{ot}}}e^{-\frac{\Delta t}{\tau_{ot}}}+\sqrt{2D}e^{-\frac{\Delta t}{\tau_{ot}}}\int_{0}^{t+\Delta t}dse^{-\frac{t-s}{\tau_{ot}}}\chi\left(s\right)\right]\\
&\times\left[r\left(0\right)e^{-\frac{t}{\tau_{ot}}}+\sqrt{2D}\int_{0}^{t}dse^{-\frac{t-s}{\tau_{ot}}}\chi\left(s\right)\right]\\
&=\langle 2De^{-2\frac{t}{\tau_{ot}}}e^{-\frac{\Delta t}{\tau_{ot}}}\int_{0}^{t}\int_{0}^{t+\Delta t}dsds'e^{\frac{s+s'}{\tau_{ot}}}\delta\left(s-s'\right)\rangle\\
&=\langle 2De^{-2\frac{t}{\tau_{ot}}}e^{-\frac{\Delta t}{\tau_{ot}}}\int_{0}^{t}dse^{2\frac{s}{\tau_{ot}}}\rangle\\
&=\langle D\tau_{ot}e^{-\frac{\Delta t}{\tau_{ot}}}\left(1-e^{-2\frac{s}{\tau_{ot}}}\right)\rangle\\
&=D\tau_{ot}e^{-\frac{\Delta t}{\tau_{ot}}}
\end{aligned} \tag{A.13}$$

Appendix B

Appendix: Power Spectral Density

In this section we derive the complete PSD predicted by the Langevin model of Brownian motion and finish by taking the overdamped approximation typical of experimental optical tweezers setups.

We start by recalling the Langevin equation in the form

$$\frac{d^2}{dt^2}\mathbf{r}(t) + f_m \frac{d}{dt}\mathbf{r}(t) + \mathbf{f}_p^2 \odot \mathbf{r}(t) = f_m\sqrt{2D}\chi(t), \tag{B.1}$$

where $f_m = \gamma/m$ and $f_{p,\mathrm{i}} = \sqrt{k_i/m}$, $\mathbf{f}_p^2 = \left[f_{p,x}^2, f_{p,y}^2, f_{p,z}^2\right]$ and $\odot$ is the element-wise Hadamard product. Performing the Fourier transform and using the property $\mathcal{F}\{\frac{d^n}{dt^n}r(t)\} = (i\omega)^n\,\tilde{\mathbf{r}}$ we have

$$\tilde{\mathbf{r}}_i = \frac{f_m\sqrt{2D}\tilde{\chi}(\omega)}{\mathbf{f}_{p,i}^2 - \omega^2 m - i\omega f_m}, \tag{B.2}$$

where $\tilde{\mathbf{r}}$ is the Fourier transform of $\mathbf{r}(t)$ in the angular frequency ω. The power spectrum is the absolute squared value of the position spectrum resulting in

$$\begin{aligned}
\mathbf{PSD}_i(\omega) = |\tilde{\mathbf{r}}_i(\omega)|^2 &= \left|\frac{f_m\sqrt{2D}\tilde{\chi}}{\tilde{\mathbf{f}}_{p,i}^2 - \omega^2 - i\omega f_m}\right|^2 \\
&= \frac{2Df_m^2}{\left(f_{p,i} - \omega^2 + i\omega f_m\right)\left(f_{p,i} - \omega^2 - i\omega f_m\right)} \\
&= \frac{2Df_m^2}{\left(f_{p,i} - \omega^2\right)^2 + \omega^2 f_m^2} \\
&= \frac{2Df_m^2}{f_{p,i}^4 + \omega^4 + \left(f_m^2 - 2f_{p,i}^2\right)\omega^2}
\end{aligned} \tag{B.3}$$

where we used the property of white noise that the power is uniform and that we had

previously normalized it $\left(|\tilde{\chi}|^2 = 1\right)$. This equation give the description of the PSD with the inertial contribution.

For the usual optical tweezers experimental setup we are far from the inertial regime. A more useful description is to consider the limit where the inertial relaxation time vanishes $(m/\gamma \to 0)$ and the PSD becomes

$$\begin{aligned} \mathbf{PSD}_i(\omega) &= \frac{2D}{\frac{\mathbf{f}_{p,i}^4}{f_m^2} + \left(\frac{m}{\gamma}\right)^2 \omega^4 + \left(1 - 2\frac{\mathbf{f}_{p,i}^2}{f_m^2}\omega^2\right)} \\ &= \frac{2D}{\left(2\pi\mathbf{f}_{c,i}^2\right)^2 + \left(1 - 2\boldsymbol{\tau}_{\mathrm{ot},i}\frac{m}{\gamma}\right)\omega^2} \end{aligned} \tag{B.4}$$

where $\mathbf{f}_{p,i}^2/f_m^2 = \mathbf{k}_i/\gamma = 2\pi\mathbf{f}_{c,i}$ and $\mathbf{f}_{p,i}^2/f_m^2 = \mathbf{k}_i m/\gamma^2 = \boldsymbol{\tau}_{\mathrm{ot}} m/\gamma$, resulting in

$$\mathbf{PSD}_i(f) = \frac{D}{2\pi^2\left(\mathbf{f}_{\mathrm{ot},i}^2 + f^2\right)}, \tag{B.5}$$

with $\omega = 2\pi f$.

Bibliography

[1] A. Ashkin, "Acceleration and trapping of particles by radiation pressure," *Physical review letters*, vol. 24, no. 4, p. 156, 1970. [Cited on pages 1 and 2.]

[2] A. Ashkin, J. M. Dziedzic, J. E. Bjorkholm, and S. Chu, "Observation of a single-beam gradient force optical trap for dielectric particles," *Optics letters*, vol. 11, no. 5, pp. 288–290, 1986. [Cited on pages 1 and 2.]

[3] A. Ashkin, "History of optical trapping and manipulation of small-neutral particle, atoms, and molecules," *IEEE Journal of Selected Topics in Quantum Electronics*, vol. 6, no. 6, pp. 841–856, 2000. [Cited on page 1.]

[4] C. Hosokawa, H. Yoshikawa, and H. Masuhara, "Cluster formation of nanoparticles in an optical trap studied by fluorescence correlation spectroscopy," *Physical Review E*, vol. 72, no. 2, p. 021408, 2005. [Cited on page 1.]

[5] A. M. Kaufman, B. J. Lester, and C. A. Regal, "Cooling a single atom in an optical tweezer to its quantum ground state," *Physical Review X*, vol. 2, no. 4, p. 041014, 2012. [Cited on page 1.]

[6] A. Ashkin and J. M. Dziedzic, "Optical trapping and manipulation of viruses and bacteria," *Science*, vol. 235, no. 4795, pp. 1517–1520, 1987. [Cited on pages 1 and 4.]

[7] I. Konyshev and A. Byvalov, "Model systems for optical trapping: The physical basis and biological applications," *Biophysical Reviews*, vol. 13, no. 4, pp. 515–529, 2021. [Cited on page 1.]

[8] J. Buajarern, L. Mitchem, A. D. Ward, N. H. Nahler, D. McGloin, and J. P. Reid, "Controlling and characterizing the coagulation of liquid aerosol droplets," *The Journal of chemical physics*, vol. 125, no. 11, p. 114506, 2006. [Cited on page 1.]

[9] Z. Gong, Y.-L. Pan, G. Videen, and C. Wang, "Optical trapping-raman spectroscopy (ot-rs) with embedded microscopy imaging for concurrent characterization and monitoring of physical and chemical properties of single particles," *Analytica Chimica Acta*, vol. 1020, pp. 86–94, 2018.

[10] R. M. Robertson-Anderson, "Optical tweezers microrheology: from the basics to advanced techniques and applications," 2018. [Cited on page 1.]

[11] C. Tuchendler, A. M. Lance, A. Browaeys, Y. R. Sortais, and P. Grangier, "Energy distribution and cooling of a single atom in an optical tweezer," *Physical Review A*, vol. 78, no. 3, p. 033425, 2008. [Cited on page 1.]

[12] T. Gustavson, A. Chikkatur, A. Leanhardt, A. Görlitz, S. Gupta, D. Pritchard, and W. Ketterle, "Transport of bose-einstein condensates with optical tweezers," *Physical Review Letters*, vol. 88, no. 2, p. 020401, 2001.

[13] A. E. Leanhardt, T. A. Pasquini, M. Saba, A. Schirotzek, Y.-i. Shin, D. Kielpinski, D. E. Pritchard, and W. Ketterle, "Cooling bose-einstein condensates below 500 picokelvin," *Science*, vol. 301, no. 5639, pp. 1513–1515, 2003.

[14] D. Stamper-Kurn, M. Andrews, A. Chikkatur, S. Inouye, H.-J. Miesner, J. Stenger, and W. Ketterle, "Optical confinement of a bose-einstein condensate," *Physical Review Letters*, vol. 80, no. 10, p. 2027, 1998. [Cited on page 1.]

[15] I. A. Carvalho, N. A. Silva, C. C. Rosa, L. C. Coelho, and P. A. Jorge, "Particle classification through the analysis of the forward scattered signal in optical tweezers," *Sensors*, vol. 21, no. 18, p. 6181, 2021. [Cited on pages 1, 6, 50, and 62.]

[16] P. A. Jorge, I. A. Carvalho, F. M. Marques, V. Pinto, P. H. Santos, S. M. Rodrigues, S. P. Faria, J. S. Paiva, and N. A. Silva, "Classification of optically trapped particles: A comparison between optical fiber tweezers and conventional setups," *Results in Optics*, vol. 5, p. 100178, 2021. [Cited on pages 1 and 6.]

[17] P. Lebedew, "Experimental investigation of the pressure of light," *The Astrophysical Journal*, vol. 15, p. 60, 1902. [Cited on page 2.]

[18] E. Nichols and G. Hull, "Pressure due to light and heat radiation," *The Astrophysical Journal*, vol. 15, p. 62, 1902. [Cited on page 2.]

[19] A. Ashkin and J. Dziedzic, "Optical levitation by radiation pressure," *Applied Physics Letters*, vol. 19, no. 8, pp. 283–285, 1971. [Cited on page 2.]

[20] A. Ashkin, "Trapping of atoms by resonance radiation pressure," *Physical Review Letters*, vol. 40, no. 12, p. 729, 1978. [Cited on page 2.]

[21] J. Liesener, M. Reicherter, T. Haist, and H. J. Tiziani, "Multi-functional optical tweezers using computer-generated holograms," *Optics Communications*, vol. 185, no. 1-3, pp. 77–82, 2000. [Cited on page 4.]

[22] J. E. Curtis, B. A. Koss, and D. G. Grier, "Dynamic holographic optical tweezers," *Optics communications*, vol. 207, no. 1-6, pp. 169–175, 2002. [Cited on page 4.]

[23] J. I. dos Santos Paiva, "Intelligent lab on fiber tools for sensing single-cells and extracellular nano-vesicles," 2019. [Cited on page 4.]

[24] I. C. Lenton, E. K. Scott, H. Rubinsztein-Dunlop, and I. A. Favre-Bulle, "Optical tweezers exploring neuroscience," *Frontiers in Bioengineering and Biotechnology*, vol. 8, p. 602797, 2020. [Cited on page 4.]

[25] R. S. R. Ribeiro, O. Soppera, A. G. Oliva, A. Guerreiro, and P. A. Jorge, "New trends on optical fiber tweezers," *Journal of Lightwave Technology*, vol. 33, no. 16, pp. 3394–3405, 2015. [Cited on page 4.]

[26] R. S. Rodrigues Ribeiro, P. Dahal, A. Guerreiro, P. A. Jorge, and J. Viegas, "Fabrication of fresnel plates on optical fibres by fib milling for optical trapping, manipulation and detection of single cells," *Scientific reports*, vol. 7, no. 1, pp. 1–14, 2017. [Cited on page 4.]

[27] X. Zhao, N. Zhao, Y. Shi, H. Xin, and B. Li, "Optical fiber tweezers: a versatile tool for optical trapping and manipulation," *Micromachines*, vol. 11, no. 2, p. 114, 2020. [Cited on page 4.]

[28] I. T. Leite, S. Turtaev, X. Jiang, M. Šiler, A. Cuschieri, P. S. J. Russell, and T. Čižmár, "Three-dimensional holographic optical manipulation through a high-numerical-aperture soft-glass multimode fibre," *Nature Photonics*, vol. 12, no. 1, pp. 33–39, 2018. [Cited on page 4.]

[29] G. Pesce, P. H. Jones, O. M. Maragò, and G. Volpe, "Optical tweezers: theory and practice," *The European Physical Journal Plus*, vol. 135, no. 12, pp. 1–38, 2020. [Cited on pages 4, 14, and 17.]

[30] N. Navon, R. P. Smith, and Z. Hadzibabic, "Quantum gases in optical boxes," *Nature Physics*, vol. 17, no. 12, pp. 1334–1341, 2021. [Cited on page 4.]

[31] Y. Yuan, Y. Lin, B. Gu, N. Panwar, S. C. Tjin, J. Song, J. Qu, and K.-T. Yong, "Optical trapping-assisted sers platform for chemical and biosensing applications: Design perspectives," *Coordination Chemistry Reviews*, vol. 339, pp. 138–152, 2017. [Cited on page 4.]

[32] A. Ashkin, J. M. Dziedzic, and T. Yamane, "Optical trapping and manipulation of single cells using infrared laser beams," *Nature*, vol. 330, no. 6150, pp. 769–771, 1987. [Cited on page 4.]

[33] M. Rasmussen, L. Oddershede, and H. Siegumfeldt, "Optical tweezers cause physiological damage to escherichia coli and listeria bacteria," *Applied and environmental microbiology*, vol. 74, no. 8, pp. 2441–2446, 2008. [Cited on page 5.]

[34] K. Svoboda and S. M. Block, "Biological applications of optical forces," *Annual review of biophysics and biomolecular structure*, vol. 23, no. 1, pp. 247–285, 1994. [Cited on page 5.]

[35] I. A. Favre-Bulle, A. B. Stilgoe, E. K. Scott, and H. Rubinsztein-Dunlop, "Optical trapping in vivo: theory, practice, and applications," *Nanophotonics*, vol. 8, no. 6, pp. 1023–1040, 2019. [Cited on page 5.]

[36] M. W. Berns, W. H. Wright, B. J. Tromberg, G. A. Profeta, J. J. Andrews, and R. J. Walter, "Use of a laser-induced optical force trap to study chromosome movement on the mitotic spindle." *Proceedings of the National Academy of Sciences*, vol. 86, no. 12, pp. 4539–4543, 1989. [Cited on page 5.]

[37] G. Volpe, L. Kurz, A. Callegari, G. Volpe, and S. Gigan, "Speckle optical tweezers: micromanipulation with random light fields," *Optics express*, vol. 22, no. 15, pp. 18 159–18 167, 2014. [Cited on pages 5, 50, and 62.]

[38] N. Malagnino, G. Pesce, A. Sasso, and E. Arimondo, "Measurements of trapping efficiency and stiffness in optical tweezers," *Optics Communications*, vol. 214, no. 1-6, pp. 15–24, 2002. [Cited on page 5.]

[39] J. Gieseler, J. R. Gomez-Solano, A. Magazzù, I. P. Castillo, L. P. García, M. Gironella-Torrent, X. Viader-Godoy, F. Ritort, G. Pesce, A. V. Arzola *et al.*, "Optical tweezers—from calibration to applications: a tutorial," *Advances in Optics and Photonics*, vol. 13, no. 1, pp. 74–241, 2021. [Cited on pages 5, 26, 28, and 65.]

[40] I. Prada, L. Amin, R. Furlan, G. Legname, C. Verderio, and D. Cojoc, "A new approach to follow a single extracellular vesicle—cell interaction using optical tweezers," *Biotechniques*, vol. 60, no. 1, p. 35, 2016. [Cited on page 5.]

[41] J. F. Marko, "Stretching must twist dna," *EPL (Europhysics Letters)*, vol. 38, no. 3, p. 183, 1997. [Cited on page 5.]

[42] J.-C. Meiners and S. R. Quake, "Femtonewton force spectroscopy of single extended dna molecules," *Physical Review Letters*, vol. 84, no. 21, p. 5014, 2000. [Cited on page 5.]

[43] E. A. Evans and D. A. Calderwood, "Forces and bond dynamics in cell adhesion," *Science*, vol. 316, no. 5828, pp. 1148–1153, 2007. [Cited on page 5.]

[44] E. Fällman, S. Schedin, J. Jass, M. Andersson, B. E. Uhlin, and O. Axner, "Optical tweezers based force measurement system for quantitating binding interactions: system design and application for the study of bacterial adhesion," *Biosensors and Bioelectronics*, vol. 19, no. 11, pp. 1429–1437, 2004. [Cited on page 5.]

[45] M. L. Bennink, S. H. Leuba, G. H. Leno, J. Zlatanova, B. G. de Grooth, and J. Greve, "Unfolding individual nucleosomes by stretching single chromatin fibers with optical tweezers," *Nature structural biology*, vol. 8, no. 7, pp. 606–610, 2001. [Cited on page 5.]

[46] M. J. Lang, P. M. Fordyce, and S. M. Block, "Combined optical trapping and single-molecule fluorescence," *Journal of biology*, vol. 2, no. 1, pp. 1–4, 2003. [Cited on page 5.]

[47] M. J. Lang, P. M. Fordyce, A. M. Engh, K. C. Neuman, and S. M. Block, "Simultaneous, coincident optical trapping and single-molecule fluorescence," *Nature methods*, vol. 1, no. 2, pp. 133–139, 2004. [Cited on page 5.]

[48] C. Xie, D. Chen, and Y.-q. Li, "Raman sorting and identification of single living microorganisms with optical tweezers," *Optics letters*, vol. 30, no. 14, pp. 1800–1802, 2005. [Cited on page 5.]

[49] T. N. Buican, M. J. Smyth, H. A. Crissman, G. C. Salzman, C. C. Stewart, and J. C. Martin, "Automated single-cell manipulation and sorting by light trapping," *Applied optics*, vol. 26, no. 24, pp. 5311–5316, 1987. [Cited on page 5.]

[50] M. M. Wang, E. Tu, D. E. Raymond, J. M. Yang, H. Zhang, N. Hagen, B. Dees, E. M. Mercer, A. H. Forster, I. Kariv *et al.*, "Microfluidic sorting of mammalian cells by optical force switching," *Nature biotechnology*, vol. 23, no. 1, pp. 83–87, 2005. [Cited on page 6.]

[51] M. P. MacDonald, G. C. Spalding, and K. Dholakia, "Microfluidic sorting in an optical lattice," *Nature*, vol. 426, no. 6965, pp. 421–424, 2003. [Cited on page 6.]

[52] X. Wang, S. Chen, M. Kong, Z. Wang, K. D. Costa, R. A. Li, and D. Sun, "Enhanced cell sorting and manipulation with combined optical tweezer and microfluidic chip technologies," *Lab on a Chip*, vol. 11, no. 21, pp. 3656–3662, 2011. [Cited on page 6.]

[53] Y. Ai, H. Alali, Y. Pan, G. Videen, and C. Wang, "Single-particle optical-trapping raman spectroscopy for the detection and identification of aerosolized airborne biological particles," *Measurement Science and Technology*, vol. 32, no. 5, p. 055207, 2021. [Cited on page 6.]

[54] Y. Liu, Z. Wang, Z. Zhou, and T. Xiong, "Analysis and comparison of machine learning methods for blood identification using single-cell laser tweezer raman spectroscopy," *Spectrochimica Acta Part A: Molecular and Biomolecular Spectroscopy*, p. 121274, 2022. [Cited on page 6.]

[55] Z. Wang, Y. Liu, W. Lu, Y. V. Fu, and Z. Zhou, "Blood identification at the single-cell level based on a combination of laser tweezers raman spectroscopy and machine learning," *Biomedical Optics Express*, vol. 12, no. 12, pp. 7568–7581, 2021. [Cited on page 6.]

[56] J. S. Paiva, P. A. Jorge, R. S. Ribeiro, M. Balmaña, D. Campos, S. Mereiter, C. Jin, N. G. Karlsson, P. Sampaio, C. A. Reis *et al.*, "ilof: An intelligent lab on fiber approach for human cancer single-cell type identification," *Scientific reports*, vol. 10, no. 1, pp. 1–16, 2020. [Cited on pages 6, 50, and 62.]

[57] L. Alzubaidi, J. Zhang, A. J. Humaidi, A. Al-Dujaili, Y. Duan, O. Al-Shamma, J. Santamaría, M. A. Fadhel, M. Al-Amidie, and L. Farhan, "Review of deep learning: Concepts, cnn architectures, challenges, applications, future directions," *Journal of big Data*, vol. 8, no. 1, pp. 1–74, 2021. [Cited on page 7.]

[58] M. Mohammadi, A. Al-Fuqaha, S. Sorour, and M. Guizani, "Deep learning for iot big data and streaming analytics: A survey," *IEEE Communications Surveys & Tutorials*, vol. 20, no. 4, pp. 2923–2960, 2018. [Cited on page 7.]

[59] R. Pascanu, T. Mikolov, and Y. Bengio, "On the difficulty of training recurrent neural networks," in *International conference on machine learning*. PMLR, 2013, pp. 1310–1318. [Cited on page 7.]

[60] L. F. Seoane, "Evolutionary aspects of reservoir computing," *Philosophical Transactions of the Royal Society B*, vol. 374, no. 1774, p. 20180377, 2019. [Cited on page 7.]

[61] M. Lukoševičius and H. Jaeger, "Reservoir computing approaches to recurrent neural network training," *Computer Science Review*, vol. 3, no. 3, pp. 127–149, 2009. [Cited on pages 8, 52, and 54.]

[62] G. Tanaka, T. Yamane, J. B. Héroux, R. Nakane, N. Kanazawa, S. Takeda, H. Numata, D. Nakano, and A. Hirose, "Recent advances in physical reservoir computing: A review," *Neural Networks*, vol. 115, pp. 100–123, 2019. [Cited on pages 8 and 52.]

[63] G. Van der Sande, D. Brunner, and M. C. Soriano, "Advances in photonic reservoir computing," *Nanophotonics*, vol. 6, no. 3, pp. 561–576, 2017. [Cited on pages 8 and 53.]

[64] Y. Paquot, F. Duport, A. Smerieri, J. Dambre, B. Schrauwen, M. Haelterman, and S. Massar, "Optoelectronic reservoir computing," *Scientific reports*, vol. 2, no. 1, pp. 1–6, 2012. [Cited on pages 8 and 54.]

[65] K. Vandoorne, J. Dambre, D. Verstraeten, B. Schrauwen, and P. Bienstman, "Parallel reservoir computing using optical amplifiers," *IEEE transactions on neural networks*, vol. 22, no. 9, pp. 1469–1481, 2011. [Cited on pages 8 and 53.]

[66] K. C. Neuman and S. M. Block, "Optical trapping," *Review of scientific instruments*, vol. 75, no. 9, pp. 2787–2809, 2004. [Cited on pages 13 and 14.]

[67] A. Ashkin, "Forces of a single-beam gradient laser trap on a dielectric sphere in the ray optics regime," *Biophysical journal*, vol. 61, no. 2, pp. 569–582, 1992. [Cited on page 13.]

[68] T. Nieminen, H. Rubinsztein-Dunlop, and N. Heckenberg, "Calculation and optical measurement of laser trapping forces on non-spherical particles," *Journal of Quantitative Spectroscopy and Radiative Transfer*, vol. 70, no. 4-6, pp. 627–637, 2001. [Cited on page 14.]

[69] T. A. Nieminen, V. L. Loke, A. B. Stilgoe, G. Knöner, A. M. Brańczyk, N. R. Heckenberg, and H. Rubinsztein-Dunlop, "Optical tweezers computational toolbox," *Journal of Optics A: Pure and Applied Optics*, vol. 9, no. 8, p. S196, 2007. [Cited on page 14.]

[70] E. Talebian and M. Talebian, "A general review on the derivation of clausius–mossotti relation," *Optik*, vol. 124, no. 16, pp. 2324–2326, 2013. [Cited on page 14.]

[71] P. H. Jones, O. M. Maragò, and G. Volpe, *Optical tweezers: Principles and applications*. Cambridge University Press, 2015. [Cited on pages 15, 17, 23, 25, and 32.]

[72] I. A. Carvalho, "Analytical tweezers for cell manipulation and diagnostic," 2021. [Cited on page 20.]

[73] S. Chandrasekhar, "Stochastic problems in physics and astronomy," *Reviews of modern physics*, vol. 15, no. 1, p. 1, 1943. [Cited on pages 23, 27, and 66.]

[74] X. Bian, C. Kim, and G. E. Karniadakis, "111 years of brownian motion," *Soft Matter*, vol. 12, no. 30, pp. 6331–6346, 2016. [Cited on pages 23 and 25.]

[75] G. E. Uhlenbeck and L. S. Ornstein, "On the theory of the brownian motion," *Physical review*, vol. 36, no. 5, p. 823, 1930. [Cited on page 24.]

[76] W. Russel, "Brownian motion of small particles suspended in liquids," *Annual Review of Fluid Mechanics*, vol. 13, no. 1, pp. 425–455, 1981. [Cited on page 25.]

[77] B. Lukić, S. Jeney, C. Tischer, A. Kulik, L. Forró, and E.-L. Florin, "Direct observation of nondiffusive motion of a brownian particle," *Physical review letters*, vol. 95, no. 16, p. 160601, 2005. [Cited on page 25.]

[78] T. Franosch, M. Grimm, M. Belushkin, F. M. Mor, G. Foffi, L. Forró, and S. Jeney, "Resonances arising from hydrodynamic memory in brownian motion," *Nature*, vol. 478, no. 7367, pp. 85–88, 2011. [Cited on page 25.]

[79] G. Volpe and G. Volpe, "Simulation of a brownian particle in an optical trap," *American Journal of Physics*, vol. 81, no. 3, pp. 224–230, 2013. [Cited on pages 32 and 33.]

[80] D. E. Rumelhart, G. E. Hinton, and R. J. Williams, "Learning representations by back-propagating errors," *nature*, vol. 323, no. 6088, pp. 533–536, 1986. [Cited on page 39.]

[81] H. Jaeger, "The "echo state" approach to analysing and training recurrent neural networks-with an erratum note," *Bonn, Germany: German National Research Center for Information Technology GMD Technical Report*, vol. 148, no. 34, p. 13, 2001. [Cited on pages 51, 53, 54, and 55.]

[82] H. Jaeger, M. Lukoševičius, D. Popovici, and U. Siewert, "Optimization and applications of echo state networks with leaky-integrator neurons," *Neural networks*, vol. 20, no. 3, pp. 335–352, 2007. [Cited on pages 53 and 54.]

[83] I. B. Yildiz, H. Jaeger, and S. J. Kiebel, "Re-visiting the echo state property," *Neural networks*, vol. 35, pp. 1–9, 2012. [Cited on page 53.]

[84] M. Buehner and P. Young, "A tighter bound for the echo state property," *IEEE transactions on neural networks*, vol. 17, no. 3, pp. 820–824, 2006. [Cited on page 53.]

[85] F. M. Bianchi, S. Scardapane, A. Uncini, A. Rizzi, and A. Sadeghian, "Prediction of telephone calls load using echo state network with exogenous variables," *Neural Networks*, vol. 71, pp. 204–213, 2015. [Cited on page 54.]

[86] F. M. Bianchi, S. Scardapane, S. Løkse, and R. Jenssen, "Reservoir computing approaches for representation and classification of multivariate time series," *IEEE transactions on neural networks and learning systems*, vol. 32, no. 5, pp. 2169–2179, 2020. [Cited on page 54.]

[87] M. Lukoševičius, "A practical guide to applying echo state networks," in *Neural networks: Tricks of the trade*. Springer, 2012, pp. 659–686. [Cited on pages 54 and 55.]